






RESEARCH ARTICLE

10.1029/2022JD038275

Climatologies of Various OH Lines From About 90,000 X-Shooter Spectra

S. Noll^{1,2} , C. Schmidt² , W. Kausch³, M. Bittner^{1,2}, and S. Kimeswenger^{3,4} 

¹Institut für Physik, Universität Augsburg, Augsburg, Germany, ²Deutsches Fernerkundungsdatenzentrum, Deutsches Zentrum für Luft- und Raumfahrt, Oberpfaffenhofen, Germany, ³Institut für Astro- und Teilchenphysik, Universität Innsbruck, Innsbruck, Austria, ⁴Instituto de Astronomía, Universidad Católica del Norte, Antofagasta, Chile

Key Points:

- Climatologies of intensity, solar cycle effect, and residual variability of 298 OH lines were derived from 10 years of X-shooter data
- The strongest variations are found for intermediate rotational energies where cold and hot OH populations show similar contributions
- Tides cause a local time shift of the climatological patterns depending on the effective line emission height

Correspondence to:

S. Noll,
stefan.noll@dlr.de

Citation:

Noll, S., Schmidt, C., Kausch, W., Bittner, M., & Kimeswenger, S. (2023). Climatologies of various OH lines from about 90,000 X-shooter spectra. *Journal of Geophysical Research: Atmospheres*, 128, e2022JD038275. <https://doi.org/10.1029/2022JD038275>

Received 28 NOV 2022

Accepted 11 APR 2023

Abstract The nocturnal mesopause region of the Earth's atmosphere radiates chemiluminescent emission from various roto-vibrational bands of hydroxyl (OH), which is therefore a good tracer of the chemistry and dynamics at the emission altitudes. Intensity variations can, for example, be caused by the general circulation, gravity waves, tides, planetary waves, and the solar activity. While the basic OH response to the different dynamical influences has been studied quite frequently, detailed comparisons of the various individual lines are still rare. Such studies can improve our understanding of the OH-related variations as each line shows a different emission profile. We have therefore used about 90,000 spectra of the X-shooter spectrograph of the Very Large Telescope at Cerro Paranal in Chile in order to study 10 years of variations of 298 OH lines. The analysis focuses on climatologies of intensity, solar cycle effect (SCE), and residual variability (especially with respect to time scales of hours and about 2 days) for day of year and local time. For a better understanding of the resulting variability patterns and the line-specific differences, we applied decomposition techniques, studied the variability depending on time scale, and calculated correlations. As a result, the mixing of thermalized and nonthermalized OH level populations clearly influences the amplitude of the variations. Moreover, the local times of the variability features shift depending on the effective line emission height, which can mainly be explained by the propagation of the migrating diurnal tide. This behavior also contributes to remarkable differences in the effective SCE.

Plain Language Summary Emission from various lines of the hydroxyl (OH) molecule is an important contribution to the Earth's nighttime radiation in the near-infrared. The emission mostly originates from altitudes between 80 and 100 km and is therefore a good tracer of the chemistry and dynamics at these altitudes. OH intensity variations can be caused by changes in the atmospheric conditions and passing waves with different time scales. In order to better understand the origin of these variations and their impact on the OH emission, we studied the variability of 298 OH lines measured in 10 years of data from the X-shooter spectrograph at Cerro Paranal in Chile. The analysis focused on average variations with respect to local time and day of year, that is, climatologies. As the lines show different vertical emission distributions, this study also provides height-dependent information. The climatologies for intensity, the response to the solar activity cycle of 11 years, and the residual variability (dominated by waves with time scales of a few hours and about 2 days) revealed remarkable patterns which depend on the OH excitation level. The features can partly be explained by the impact of solar tides, particularly with a period of 24 hr.

1. Introduction

Chemiluminescent emission of the hydroxyl (OH) radical dominates the nocturnal radiation of the Earth's atmosphere in the near-infrared wavelength regime. Various roto-vibrational bands of the electronic ground state contribute to the emission spectrum (e.g., Noll et al., 2015; Rousselot et al., 2000). The radiation originates in the mesopause region between 80 and 100 km (e.g., Baker & Stair, 1988; Noll et al., 2022b) and is mostly related to the production of OH with relatively high vibrational excitation (up to a vibrational level $v = 9$) by the reaction of atomic hydrogen and ozone (Bates & Nicolet, 1950) and the subsequent relaxation processes. Apart from the emission of photons, collisions with different constituents of the atmosphere contribute to this redistribution of the level populations. In the end, the population of each v can be described by a cold, fully thermalized and a hot, nonthermalized component (Kalogerakis et al., 2018; Noll et al., 2020; Oliva et al., 2015). The latter dominates the populations of levels with high rotational quantum numbers N .

© 2023. The Authors.

This is an open access article under the terms of the [Creative Commons Attribution License](https://creativecommons.org/licenses/by/4.0/), which permits use, distribution and reproduction in any medium, provided the original work is properly cited.

The OH emission layer with a typical full width at half maximum of about 8 km (Baker & Stair, 1988) can be affected by perturbations in pressure, temperature, and the distribution of the atmospheric constituents on different time scales as such changes alter the production and thermalization of OH molecules. In particular, atomic oxygen matters. This radical is required for the production of ozone and plays an important role in the vibrational relaxation and destruction of OH (e.g., Adler-Golden, 1997; Dodd et al., 1994; Noll et al., 2018b; von Savigny et al., 2012). It shows a strong response to vertical transport since its concentration steeply declines in the lower part of the OH emission region (e.g., Smith et al., 2010), where the buildup of a reservoir by photolysis of molecular oxygen at daytime is less efficient and the consumption of atomic oxygen at nighttime is fast under undisturbed conditions (Marsh et al., 2006). An important source of perturbation are the globally acting solar tides, especially the westward migrating diurnal and semidiurnal tides (e.g., Smith, 2012), which propagate from the troposphere/stratosphere into the mesopause region (e.g., Hagan et al., 1995). The related changes in the vertical pressure, temperature, and chemical composition profiles can significantly alter the nocturnal trend in OH emission, that is, emission increases are also possible (e.g., Marsh et al., 2006; Takahashi et al., 1998; Zhang et al., 2001). Intra-annual changes in the tidal amplitudes also contribute to the observed seasonal variability of OH emission with maximum intensities around the equinoxes at low latitudes (e.g., Gao et al., 2010; Shepherd et al., 2006; Takahashi et al., 1995). Another source of perturbations of the mesopause region are gravity waves (GWs), which have periods from minutes to hours and act on a regional scale (e.g., Fritts & Alexander, 2003). Individual GWs are sporadic but the general activity of such waves with respect to OH emission shows a seasonal pattern (e.g., Hannawald et al., 2019; Kim et al., 2010; López-González et al., 2020; Reisin & Scheer, 2004; Sedlak et al., 2020). Increased activity tends to be observed around solstices or in winter depending on the wave period and the latitude. The intra-annual variations are related to the weather conditions in the troposphere (the dominating source region for primary waves) and the wind speeds and directions up to the mesosphere. The latter rule the efficiency of the blocking of the vertical wave propagation and the related possible generation of secondary waves. OH emission is also influenced by the globally acting planetary waves with periods of the order of days (e.g., López-González et al., 2009; Pedatella & Forbes, 2012) and the seasonal changes of the residual meridional circulation (e.g., Marsh et al., 2006). Changes in OH nightglow on time scales of the order of years are particularly caused by the solar activity cycle of about 11 years (e.g., Gao et al., 2016; Noll et al., 2017), which leads to a significant variation of hard ultraviolet photons that can, for example, destroy molecular oxygen (e.g., Marsh et al., 2007).

In conclusion, the sensitivity of OH lines to the various sources of variation makes them valuable for the study of the dynamics in the mesopause region. However, the investigations are often based on a few bright lines or unresolved broad-band data due to instrumental limitations. This constitutes a loss of information. As the radiative lifetimes and rate coefficients for collisions depend on the specific OH energy level, the vertical emission distributions deviate for OH lines with different upper levels (e.g., Dodd et al., 1994; Noll et al., 2018b; von Savigny et al., 2012). Consequently, the response of OH emission to perturbations depends on the selected line. The resulting differences can therefore provide additional information on the vertical component of the dynamics as well as the OH-related chemistry. At least for the integrated intensities of the Q branches of OH(3-1) and OH(4-2), this was demonstrated by Schmidt et al. (2018), who estimated vertical wavelengths of GWs. Studies of large sets of individual OH lines are rare, particularly with respect to variations. With a few thousand spectra in maximum (Cosby & Slanger, 2007; Hart, 2019; Noll et al., 2015, 2017), only a rough characterization of the dynamics was possible. Some differences in the nocturnal, seasonal, and long-term variations for lines with different upper vibrational levels v' were identified. A fraction of these variations might be explained by differences in the thermalization of the involved level populations as the observed changes in the rotational and vibrational temperatures, that is, ratios of lines with different upper levels N' and v' , indicate. The studies did not involve weak lines with high N' , which would be crucial for a better understanding of the variation of the level populations on different time scales especially with respect to the hot component.

In a previous study (Noll et al., 2022b), we analyzed 298 OH lines with a wide range of v' and N' . The intensities were measured in spectra of the X-shooter spectrograph (Vernet et al., 2011) of the Very Large Telescope (VLT) of the European Southern Observatory (ESO) at Cerro Paranal in Chile (24.6°S, 70.4°W). In a time interval of eight nights in January/February 2017 (and also seven nights in January 2019), the data set allowed us to perform a detailed study of the propagation of a very strong (and a moderate) quasi-2-day wave (Q2DW), which is the most remarkable planetary wave at low southern latitudes (e.g., Ern et al., 2013; Gu et al., 2019; Tunbridge et al., 2011). It is characterized by a lifetime of only a few weeks usually in summer and a westward moving

pattern with a zonal wavenumber of 3 in the southern hemisphere. Our fits of the wave properties resulted in a most likely period of 44 hr for both events, a strong dependence of the wave amplitude on local time (LT) in 2017 mainly due to the interaction of the Q2DW with solar tides, and maximum amplitudes for lines with intermediate N' in both years. As the latter show similar contributions of cold and hot populations (Noll et al., 2020), the increased intensity variability can be explained by variations in the ambient temperature that significantly affect the population mixing. In combination with emission profiles of the two OH channels of the Sounding of the Atmosphere using Broadband Emission Radiometry (SABER) instrument onboard the Thermosphere Ionosphere Mesosphere Energetics Dynamics satellite (Russell et al., 1999), we linked wave phases and emission heights for the wave in 2017 thanks to a nearly linear relation and significant phase differences. With a vertical wavelength of about 32 km, we finally derived average centroid emission heights between 86 and 94 km. The emission altitudes increase with v' and N' .

These results demonstrate the potential of parallel investigations of the dynamics of various OH lines. In this study, we extend the analysis of the same 298 lines by using the entire X-shooter data set discussed by Noll et al. (2022b) of about 90,000 near-infrared spectra covering a period of 10 years between October 2009 and September 2019. The resulting wealth of data allowed us to study climatologies for LT and day of year for the intensity, solar cycle effect (SCE), and residual variability in order to characterize the impact of the OH level on the intensity variation for perturbations with different time scales. The contents of the paper are as follows. First, we will briefly describe the data set (Section 2). Then, we will introduce our approach to calculate the climatologies and our decomposition techniques for a detailed analysis (Section 3). The results for the different investigated properties will be discussed in Section 4. Finally, we will draw our conclusions (Section 5).

2. Data

We used VLT/X-shooter spectra in the near-infrared between 1.0 and 2.5 μm (Vernet et al., 2011) taken in a time interval of 10 years. In the following, we give a brief overview of the related data processing and data selection. More details are provided by Noll et al. (2022b).

The raw medium-resolution echelle spectra of astronomical targets originate from the ESO Science Archive Facility and were first processed with version v2.6.8 of the official reduction pipeline (Modigliani et al., 2010) and preprocessed calibration data. The resulting wavelength-calibrated two-dimensional (2D) spectra were then further treated by averaging them along the spatial direction (projected slit length of 11"), correcting them for systematic biases in the pipeline-based separation of sky and astronomical target, and performing an absolute flux calibration based on 10 master response curves with valid time intervals between 9 and 15 months that were derived from X-shooter spectra of the spectrophotometric standard stars Eggen and Greenstein 274 and Luyton's Two Tenth 3218 (Moehler et al., 2014). For the predominating clear sky conditions, the relative flux uncertainties are expected to be of the order of 2%–3% for wavelengths up to 2.1 μm . The accuracy of the absolute fluxes is lower due to uncertainties in the reference spectral energy distributions of the standard stars.

In the final spectra, the continuum was determined by means of the lowest quintile of the intensities in pixel ranges that depended on the corresponding line density and slope of the continuum. After the subtraction of the continuum, line intensities were measured in wavelength ranges which depended on the variable width of the entrance slit of the spectrograph and the separation of the Λ doublet components of each OH line as taken from Brooke et al. (2016). The measured line intensities were corrected for their dependence on the zenith angle due to projection effects assuming a reference altitude of 87 km. Moreover, we considered the partial absorption of line emission by molecules especially in the lower atmosphere. The line-specific absorption was modeled for Doppler-broadened OH lines assuming a temperature of 190 K and by means of the Line-By-Line Radiative Transfer Model (LBLRTM, Clough et al., 2005), which involved typical atmospheric profiles for Cerro Paranal (Noll et al., 2012). Apart from the line, the correction depended on the zenith angle and the highly variable amount of water vapor. The latter was estimated based on pairs of OH lines with very different absorption. The relations were calibrated using data of the Low Humidity And Temperature PROfiler microwave radiometer at Cerro Paranal (Kerber et al., 2012). For this study, we used the same 298 OH lines as selected for the analysis of the Q2DW in 2017 by Noll et al. (2022b). In this way, we can directly compare both investigations. Moreover, the results suggest that an additional optimization of the line set for the studied climatological properties would not significantly improve the quality of the analysis. Selection criteria such as high atmospheric transmission,

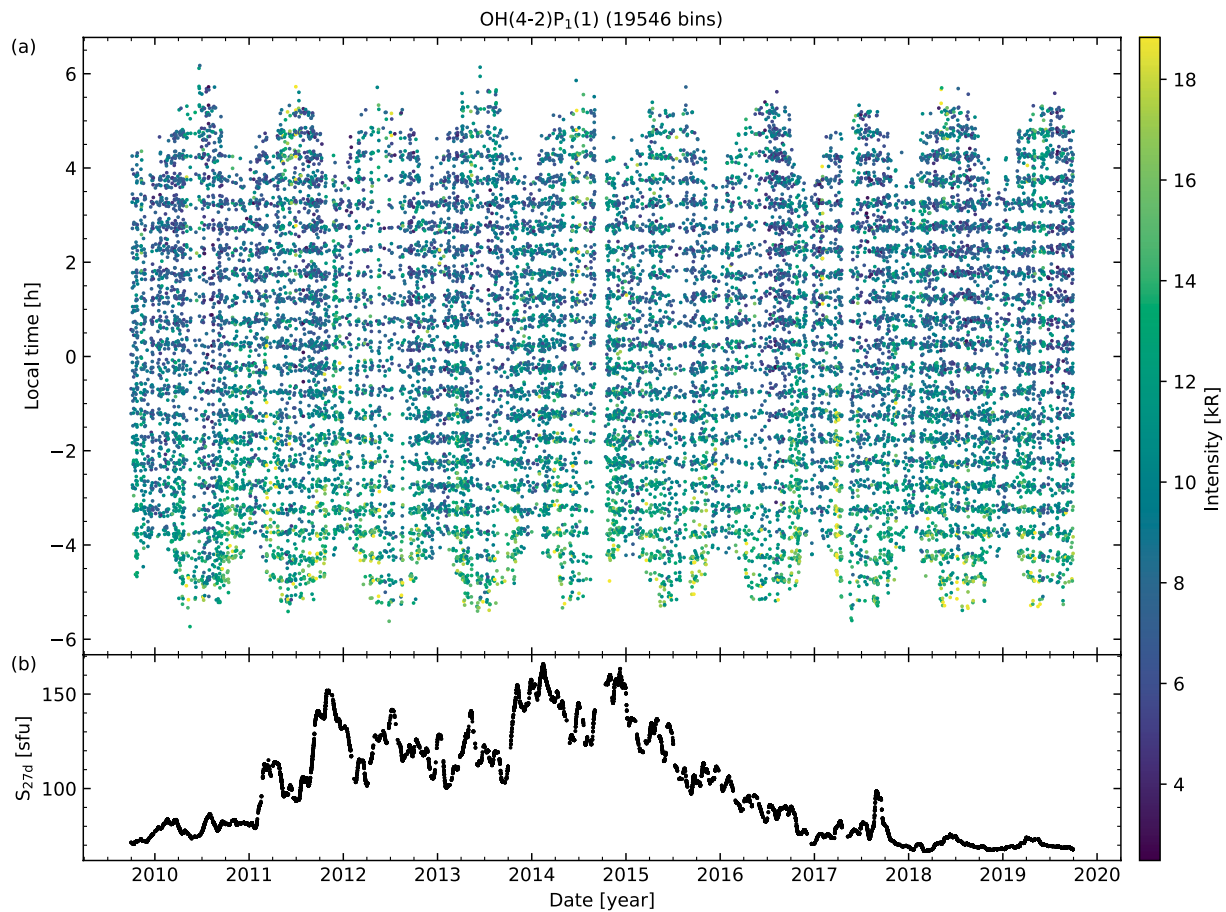


Figure 1. Sampling of date in years and local time (LT) in hours for the 19,546 30 min bins used for OH(4-2)P₁(1) (a). The given times of each LT interval differ due to the different central times and exposure lengths of the contributing individual observations. (a) Also provides the mean intensities of the bins in kilorayleigh (kR). For a better visibility of the variations, the upper limit of the color scale was fixed to 3 standard deviations above the mean intensity. This cut only affected 132 bins. (b) Shows the sampling of the solar radio flux at 10.7 cm averaged for 27 days, S_{27d} , in solar flux units (sfu). The distribution indicates that the most of solar cycle 24 is covered.

negligible line blending, and smooth underlying continuum work independently of the data sample and the analyzed property.

As the individual spectra show strong variations in the exposure time, spectral resolution, absorption by water vapor, zenith angle, and residual contribution of the astronomical target, the size of the useful data set depends on OH line properties such as intensity and wavelength. Based on a σ -clipping approach for outlier detection with respect to continuum, intensity, and intensity uncertainty, the final line-specific samples comprise between 61,458 and 88,315 data points with a mean of 82,836 for the 298 lines. In order to further improve the quality, we averaged the intensities for consecutive 30 min intervals and only kept those intervals with a minimum summed exposure time of 10 min. This approach significantly reduced the variation in the size of the data set. For the 268 OH lines with wavelengths up to 2.1 μm , the resulting number of bins is between 18,936 and 19,570 (mean of 19,480 and relative standard deviation of 0.65%). The corresponding data coverage with respect to date and LT is illustrated in Figure 1a for an example line. In general, there is a relatively smooth coverage as 63% of the nights are covered with an average number of 8.5 bins. Data gaps longer than a week are rare (maximum of 41 consecutive nights in 2014). As bad weather is a minor issue at Cerro Paranal (Holzlöhner et al., 2021; Kerber et al., 2016), technical reasons are more common (especially telescope sharing by different instruments). In the case of the 30 lines at longer wavelengths (mainly belonging to OH(9-7)), the bin numbers range from 16,926 to 17,019 (mean of 17,001 and relative standard deviation of 0.10%). Hence, the only noteworthy differences are related to the wavelength regime. Spectra taken with a so-called *K*-blocking filter for straylight reduction (Vernet et al., 2011) cannot be used beyond 2.1 μm . Nevertheless, the decrease of the sample size at long wavelengths is

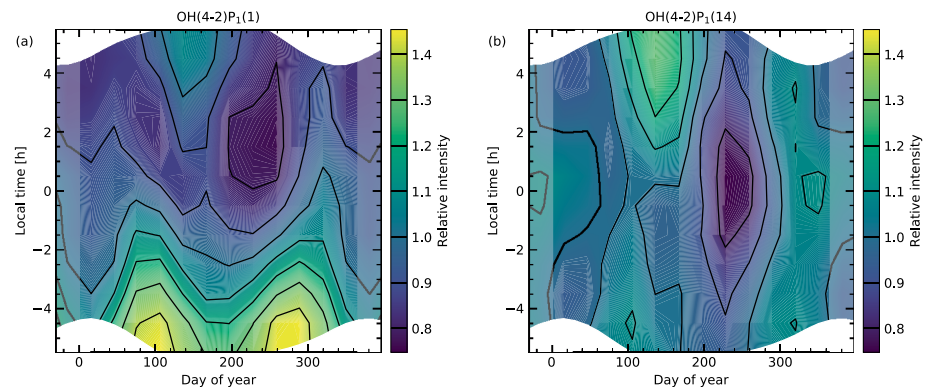


Figure 2. Climatologies of intensity relative to mean as a function of local time (with a resolution of 1 hr) and day of year (with a resolution of 1 month) for OH(4-2) $P_1(1)$ (a) and OH(4-2) $P_1(14)$ (b). The climatologies are representative of a solar radio flux of 100 sfu. The colored contours are only provided for dates and times with solar zenith angles larger than 100° . The seasonal variation is partly repeated (marked by lighter colors) for a better representation around the turn of the year.

only about 13%. Hence, the resulting climatologies should still be sufficiently consistent. Comparisons for $\nu' = 9$ lines from different bands did not show clear discrepancies.

3. Methods

3.1. Calculation of Climatologies

In this study, we focus on 2D climatologies depending on local time (LT) and day of year (e.g., Figure 2). The LT is defined as mean solar time for the longitude of Cerro Paranal (70.4°W). Each climatology consists of a grid of 12×12 data points with centers in the middle of the nighttime hours (from 18:30 to 05:30 LT) and the middle of the months. Each grid point represents the average of a property for a selection of close data bins, which were derived as discussed in Section 2 and are representative of the average of the central times of the considered individual exposures weighted by the exposure time (see Figure 1a). The maximum relative distance to a grid point was usually 1.0, which corresponds to time differences of 1 hr and 1 month of average length, respectively. Hence, a bin can contribute to several adjacent grid points. The climatologies are smoothed. Smaller selection radii would lead to a better time resolution but worse statistics. We required a minimum number of selected bins of 400. Even if we only consider the 134 grid cells with significant nighttime contribution (at least 24% with respect to solar zenith angles greater than 100°) that were used for the scientific analysis, this criterion is not always fulfilled. In such cases, we iteratively increased the selection radius in steps of 0.1 until the sample was large enough. For the example line OH(4-2) $P_1(1)$ (see also Noll et al., 2022b), where the input data set and the resulting intensity climatology are shown in Figures 1 and 2a, the mean radius was 1.10 for the 134 useful grid points. However, it was only 1.02 for the 113 cells with 100% nighttime contribution. The mean sample size was 522 with a maximum of 732. Apart from the decrease of the numbers close to twilight, the sample size shows a remarkable seasonal pattern with maximum numbers around the equinoxes. These variations reflect changes in the structure of the X-shooter observing programs, which depend on the seasonal visibility of the different classes of astronomical objects. As discussed in Section 2, the number of data bins is significantly reduced for OH lines with wavelengths longer than $2.1 \mu\text{m}$. Nevertheless, the time resolution and quality of the statistics is only slightly worse. For OH(9-7) $P_1(1)$, we find a mean selection radius of 1.14 and a mean sample size of 474 for the 134 useful grid points.

Intensity climatologies relative to the mean as shown in Figure 2 were corrected for time-specific differences in the mean solar radio flux at 10.7 cm (Tapping, 2013). As OH intensities depend on solar activity (e.g., Gao et al., 2016; Noll et al., 2017), variations in the mean solar radio flux by the selection of subsamples can affect intensity climatologies. Using the moving 27-day average centered on the day of observation, S_{27d} (see Figure 1b), as preferred by Noll et al. (2017), we found values between 89 and 109 solar flux units (sfu) with a mean of 99 sfu for the nighttime grid points related to the representative example OH(4-2) $P_1(1)$. The mean S_{27d} values are relatively low in July/August and relatively high in November/December. In order to minimize the impact of the solar radio flux on the intensity climatologies, we corrected the intensities of each grid point to be representative

of 100 sfu, which is close to the mean value. For this purpose, we performed a linear regression analysis for the relation between intensity and solar radio flux. The resulting slopes for the different subsamples were then used for the correction. The climatologies of these slopes are discussed in Section 4.2. As a standard deviation of 5 sfu is relatively small, the correction factors only varied between 0.98 and 1.04 with a standard deviation of 0.01 for OH(4-2) $P_1(1)$. The lowest and highest factors were found in December and July, respectively. The approach led to a general decrease of the variance in the selected subsamples. Average reductions between 1% and 6% were found for the climatologies of the different lines.

3.2. Decomposition of Climatologies

For a systematic analysis of the climatologies of different properties for the whole set of selected OH lines, we used decomposition techniques. First, we performed the popular principal component analysis (PCA), which is an orthogonal linear transformation in the feature space that results in a new coordinate system with the maximum sample variance along the primary axis, the second largest variance along the orthogonal secondary axis, and so on. Consequently, a few dimensions are sufficient to describe most of the variance, which significantly reduces the complexity of the data set. The most important variability patterns are highlighted, whereas the contribution of noise and outliers is minimized. The transformation can be written as

$$\mathbf{T} = \mathbf{X}\mathbf{W}. \quad (1)$$

This matrix equation includes the matrix of the input data \mathbf{X} with n rows representing the samples and p columns representing the features. In our case, p equals 298, that is, the number of selected OH lines, and n is 134, that is, the number of useful nighttime data points of the climatologies (see Section 3.1). Note that the sample mean of each column (the individual climatologies) needs to be shifted to zero before the PCA can be applied. For a complete transformation, the weight matrix \mathbf{W} and the score matrix \mathbf{T} would have sizes of $p \times p$ and $n \times p$, respectively. However, as we aim at reducing the dimensionality, these matrices are truncated with sizes of $p \times L$ and $n \times L$, where L is the number of kept dimensions. Our analysis showed that it is sufficient to choose $L = 2$ as the explained variance is already between 89% and 98% depending on the property (see also Section 4). Moreover, the third and higher components indicated that they were strongly affected by variability caused by measurement uncertainties. The climatologies of all 298 lines (set to mean values of zero) can then be described by the linear combination of two basis climatologies provided by the columns of \mathbf{T} and the corresponding scaling factors for each line given by \mathbf{W} .

Apart from PCA, we also used nonnegative matrix factorization (NMF; e.g., Lee & Seung, 1999) for the analysis of the different climatologies. NMF is an approximative dimensionality reduction of the form

$$\mathbf{A}\mathbf{B} \approx \mathbf{X}, \quad (2)$$

where all matrices have only nonnegative entries. The input data matrix \mathbf{X} with n rows and p columns is the same as discussed above. The result matrices \mathbf{A} and \mathbf{B} have sizes of $n \times L$ and $L \times p$, that is, they provide the basis climatologies and line-dependent scaling coefficients for the approximative reconstruction of the individual climatologies. Consistent with the PCA, we selected $L = 2$ for the simplest description of the variability. Note that the choice of L affects the patterns of the basis climatologies, whereas the PCA-related components remain fixed independent of L . In general, the NMF-related results were similar to those of the PCA, even in the case of the SCE, where the possible negative values had to be set to zero for the application of the NMF. The corresponding systematic bias was relatively small as only a small fraction of slightly negative values contributed to the different climatologies. Nevertheless, we preferred the unbiased PCA for this analysis. The PCA-related results dominate the discussion in Section 4. The only exception is Section 4.1 on intensity climatologies as the NMF-related separation of the two main contributions was significantly better, which motivated us to also include that approach in our analysis. The results of both methods are available via the release of the full data set (Noll et al., 2023).

3.3. Variability as a Function of Time Scale

Our analysis also comprises a study of the variations which are not covered by the 2D climatologies of intensity and SCE. This residual variability (Section 4.3) can be caused by intensity changes on different time scales. For the interpretation, it is therefore important to understand the contributions of the different wave types depending

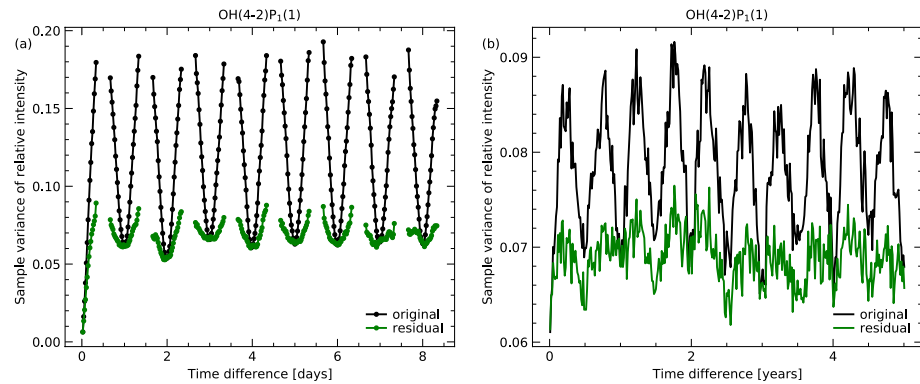


Figure 3. Sample variance derived from data pairs as a function of the pair-related time difference Δt for intensity relative to mean of OH(4-2)P₁(1) (black) and the latter after subtraction of the solar-activity-adapted (Section 3.1) climatology in Figure 2a (green/gray). (a) Shows the variance for Δt of the order of hours and days with a time resolution of 30 min (marked by dots), that is, the step size of the binned input data. Time differences that are rare due to the restriction to nighttime data are skipped. (b) Displays the results for Δt of multiples of full days up to 5 years. For a smoother plot, only the averages of bins with a width of 5 days are shown.

on the climatological grid point. As the X-shooter data set is highly inhomogeneous, this analysis requires a robust approach with respect to data gaps. A promising statistical method is the study of intensity differences between all possible combinations of data pairs as a function of the corresponding time difference. As the time series consist of bins with a width of half an hour (Section 2), we can assign each pair of relative intensities I_i and I_j to a time difference $\Delta t = t_i - t_j$ which is a whole-number multiple of 30 min. Then, we can calculate the mean sample variance

$$s^2(\Delta t) = \frac{1}{N(\Delta t)} \sum_{\Delta t, i > j} s_{ij}^2 \quad \text{with} \quad s_{ij} = \frac{|I_i - I_j|}{\sqrt{2}} \quad (3)$$

for the $N(\Delta t)$ pairs of each Δt . Without restrictions in Δt , it would equal the normal sample variance based on deviations from the mean value of the full data set. Moreover, the definition has the advantages that pure noise with a Gaussian distribution causes a constant shift of σ^2 and that a sine wave with the period T results in an oscillation between 0 (achieved for integer multiples of T) and the squared amplitude a^2 (shifted by half a period).

In order to illustrate the approach, Figure 3 shows $s^2(\Delta t)$ for the intensities relative to the mean for our example line OH(4-2)P₁(1) based on the full number of 19,546 useful bins. The function is given for relatively short Δt up to 8.5 days (a) and longer time scales up to 5 years with a step size of 5 days (b). For the latter case, only s^2 for integer multiples of 1 day were averaged. There is a dominating oscillation with a period of 24 hr, which reflects the strong nocturnal trend in Figure 2a. Moreover, a clear semi-annual oscillation is visible, which mainly originates from the climatological pattern at the beginning of the night. As we are primarily interested in the residual variability, the 2D intensity climatology for 100 sfu in Figure 2a adapted to the actual S_{27d} values (Section 3.1) was subtracted from the times series. The results are also shown in Figure 3. As expected, $s^2(\Delta t)$ of the corrected time series indicates distinctly lower variances. Exceptions in Figure 3a are only present for time scales of a few hours and multiples of 24 hr. They reveal the importance of short-term variations and day-to-day variations of the nocturnal pattern for the residual variability. For long time scales, the lowest reduction can be seen for multiples of 1 year. Hence, year-to-year variations are probably more crucial for the annual oscillation, which dominates the second half of the night in Figure 2a.

The analysis can also be performed for each grid point of the 2D climatology. In this way, the contributions of the different time scales to the residual variability climatology can be studied in detail. As only a small fraction of the entire data set is relevant for a specific grid point (see Section 3.1), there can be a lack of suitable pairs for a certain Δt . This issue affects long time scales in general as well as short times scales where the absence of daytime data matters. Good statistics are therefore limited to Δt of a few hours and those close to low multiples of 24 hr. These restrictions still allow the detailed study of the impact of short-term variations with time scales shorter than 1 day, which constitute the largest contribution to the residual variability as Figure 3a reveals. For maximum robustness, we measured the short-term variance as the minimum of s^2 for Δt of 24 and 48 hr. In the

case of the whole time series of OH(4-2) $P_1(1)$, the variance for 48 hr is clearly lower. This fact suggests that there is a significant contribution of the Q2DW, although its activity period is usually only a few weeks in summer (e.g., Ern et al., 2013). Consequently, we can also estimate the amplitude of the Q2DW. Assuming a sine wave, we derived a^2 by subtracting s^2 for 48 hr from the mean for 24 and 72 hr. In the case of a negative difference, we set $a = 0$. This approach may lose a part of the amplitude as the Q2DW period can deviate from 48 hr. Noll et al. (2022b) found 44 hr for the covered intervals in 2017 and 2019 at Cerro Paranal. However, the restriction to multiples of 24 hr increases the robustness of the statistics and avoids possible biases depending on LT due to different influences of daytime intervals without observations. Concerning the statistics, $\Delta t = 72$ hr is the time difference with the lowest number of data pairs. For the nocturnal grid points of the climatology of OH(4-2) $P_1(1)$, we find numbers between 88 and 300 with a mean of 172, that is, about one third of the average sample size. In conclusion, our analysis allows us to study 2D climatologies of short-term variations and Q2DW amplitudes. The corresponding results will be discussed in Sections 4.3.1 and 4.3.2.

4. Results

4.1. Relative Intensity

Figure 2 shows example climatologies of intensity relative to the climatological mean for a solar radio flux of 100 sfu and solar zenith angles greater than 100° . Both example lines belong to the P_1 branch of the strong OH(4-2) band but show the maximum difference in the upper rotational quantum number N' of the line set (1 vs. 14). The reference intensities for the two climatologies are 9.65 and 0.18 kR, respectively. Hence, even the high- N' line is still relatively bright. The mean intensity is comparable to those of the green and red atomic oxygen lines at Cerro Paranal (Noll et al., 2012). The derived intensity climatologies appear to be quite robust since the relative root mean square averaged for the climatologies of the 23 lines with $N' \geq 10$ (mean intensities between 7 and 570 R) is only 2.5%, irrespective of possible true physical differences. The comparison of both climatologies in Figure 2 reveals clear differences at the beginning of the night, where OH(4-2) $P_1(1)$ shows much stronger emission relative to the mean. The maximum values near both equinoxes (April and October) are hardly visible in the climatology of OH(4-2) $P_1(14)$. The maximum in the second half of the year even appears to be shifted to November. On the other hand, the patterns after midnight are more similar. In particular, the maximum in May before dawn and the minimum in August/September can be found in both climatologies. A 2D intensity climatology for Cerro Paranal was already shown by Noll et al. (2017) for P-branch lines with low N' in OH(6-2). The summed intensity of these lines indicates a variability pattern that agrees quite well with our results for OH(4-2) $P_1(1)$. The data of Noll et al. (2017) were taken between April 2000 and March 2015 with another VLT spectrograph. Moreover, similar features as in Figure 2a are also present in the nocturnal trends and monthly variations of the OH(9-4) band (dominated by lines with low N') measured by Takahashi et al. (1998) at Cachoeira Paulista in Brazil (23°S , 45°W) for the period between October 1987 and June 1993. The 2D climatology of the OH(8-3) band at Buckland Park in Australia (35°S , 139°E) for the years 1995–2010 from Reid et al. (2014) also indicates a rough agreement. Consequently, the shown intensity climatologies appear to be relatively stable with respect to the observing period and moderate changes of the latitude. For larger changes of the latter, there can be significant deviations as a SABER-based study of the global OH peak emission rates by Gao et al. (2010) suggests. The impact of the latitude is also illustrated by the study of Takahashi et al. (1998), which also contains results for a site close to the equator (4°S).

Our data set particularly benefits from the parallel coverage of hundreds of OH lines which show differences in their effective emission heights of several kilometers (Noll et al., 2022b). Therefore, more detailed insights into the OH-related dynamics will be possible if the climatologies of all 298 lines are jointly studied in a systematic way. For this purpose, we applied the decomposition techniques that were introduced in Section 3.2. The first two components of the PCA (matrix \mathbf{T} in Section 3.2) explain 98.4% of the full variance. The first component is similar to the intensity climatology of OH(4-2) $P_1(1)$, whereas the second one better agrees with the climatology of OH(4-2) $P_1(14)$. This result confirms that the variabilities of our example lines differ relatively strongly with respect to the full line set. The PCA was not able to properly separate the high intensities at the beginning of the night, which are only visible for one example line, from the other variability features that can be found in the data of both lines. As stated in Section 3.2, we therefore preferred the NMF. It works particularly well if a pattern can be reconstructed by summing a few nonnegative components. For our analysis, we calculated the decomposition for the least complex case, that is, two components.

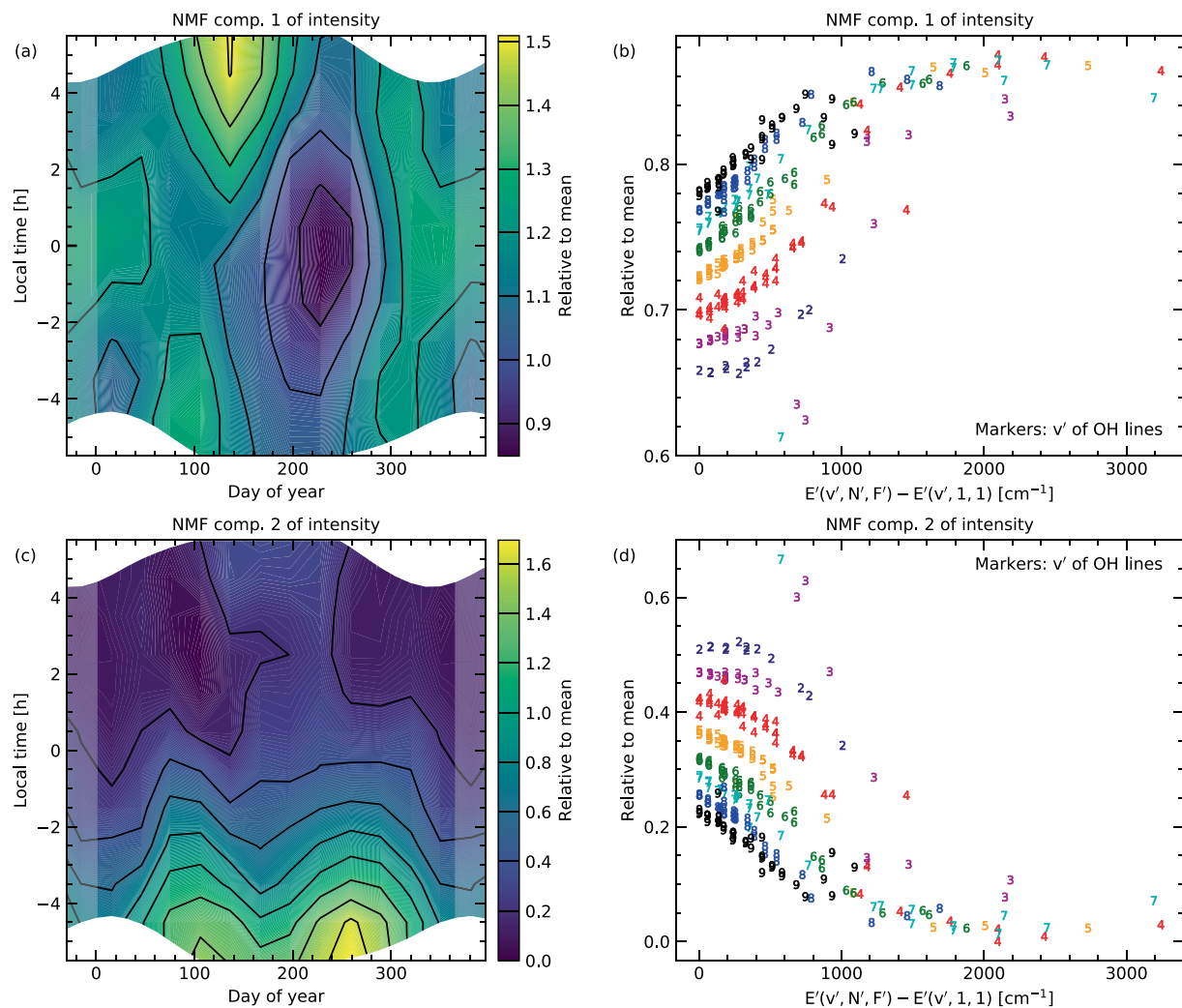


Figure 4. Decomposition of climatologies of intensity relative to mean with nonnegative matrix factorization for two components. The resulting climatologies (see also Figure 2) as given by matrix **A** in Section 3.2 are shown in (a) and (c) and the corresponding coefficients for the 298 considered OH lines from matrix **B** are given in (b) and (d). The number symbols in the latter plots indicate the upper vibrational level of the transition v' . The abscissa shows the energy of the upper level of the transition minus the lowest energy for the corresponding v' in inverse centimeters. The additional energy is related to rotation with quantum numbers $N' > 1$ and/or spin-orbit coupling with quantum number $F' = 2$ (see Noll et al., 2020).

A comparison of the resulting basis climatologies in the left column of Figure 4 (matrix **A** in Section 3.2) with the example cases in Figure 2 shows that the NMF clearly separates the strongly line-dependent nocturnal trend of decreasing intensities from the underlying features that are obviously present in all climatologies. The latter are characterized by the first component in Figure 4a, which is very similar to the climatology of OH(4-2) P_1 (14). The correlation coefficient r for the climatological grid cells with significant nighttime contribution is +0.94. For the interpretation of this remarkable pattern with the maximum in May at 05:30 LT and the minimum in August at 23:30 LT, it is important to know whether it is restricted to OH intensities or whether it can also be seen in other properties of the mesopause region. The kinetic temperature is a popular quantity for the study of mesospheric perturbations. It can be estimated from intensity ratios of OH lines if the involved level populations are in local thermodynamic equilibrium, which is best fulfilled for the lowest v' and N' (Cosby & Slanger, 2007; Kalogerakis et al., 2018; Noll et al., 2015, 2016, 2020). We therefore analyzed the ratio of the P_1 lines of OH(3-1) with $N' = 1$ and 2, which are frequently used for airglow instruments optimized for temperature measurements (e.g., Schmidt et al., 2013). The climatology of the line ratio indicates a good correlation with the first NMF component ($r = +0.83$). There are no increased values in the evening as it is typical of individual lines with low v' and N' like OH(4-2) P_1 (1) (Figure 2a). This result is also confirmed by the 2D climatology of kinetic

temperature based on SABER measurements at 89 km in the region of Cerro Paranal from Noll et al. (2019). The same publication shows that similar features are also present for the number density of atomic oxygen, which is crucial for the production of OH. Hence, the first NMF component is an indicator of general perturbations of the mesopause region. As the climatologies amplify variations with fixed time scales of 24, 12, or 8 hr, solar tides and the seasonal changes of their amplitudes appear to be the main source of the variability pattern. The significant impact of tides on OH emission was already discussed before (e.g., Marsh et al., 2006; Takahashi et al., 1998; Zhang et al., 2001). It is especially important for low latitudes where the migrating diurnal tide that follows the apparent motion of the Sun is the most prominent mode. The residual meridional circulation that can influence the seasonal variability appears to be a minor effect at low latitudes (Marsh et al., 2006).

The second NMF-related basis climatology is shown in Figure 4c. In each month, the intensity is decreasing in the course of the night with the highest rates in the evening. Moreover, the pattern indicates a semi-annual oscillation with the maximum values near the equinoxes (April and September). The latter could be related to the ozone number density in the OH emission layer, which indicates a similar seasonal variation (Noll et al., 2019). As the nocturnal decrease is not visible in the climatologies of kinetic temperature and atomic oxygen number density shown by Noll et al. (2019), the phenomenon seems to be linked to the OH-related chemistry. As already discussed by Marsh et al. (2006), the drop in intensity is probably caused by the consumption of atomic oxygen, which is mostly produced at daytime due to photolysis of molecular oxygen. In the denser atmosphere at lower altitudes, the losses (also by the production of OH via ozone) are faster. Assuming an exponential decay, Marsh et al. (2006) modeled time constants of 6 hr at 84 km and 1 day at 88 km, which indicates a large vertical gradient of this property. We can also fit exponential functions in the second NMF component. For the natural logarithm of the values, only a linear regression analysis needs to be performed. For a better robustness, we only considered local times until the nocturnal minimum and only grid points with relative intensities higher than 0.04. The average of all monthly fits amounts to 3.3 ± 0.2 hr, which suggests that the crucial altitudes are probably 1–3 km below 84 km (if the model of Marsh et al. works for our data). Emission at higher altitudes with long decay times appears to mainly contribute to the first basis climatology in Figure 4a. The second NMF component is therefore strongest for OH lines with the lowest effective emission heights, which are about 86 km on average (Noll et al., 2022b) but could be about 2 km lower in the early evening as SABER data for Cerro Paranal indicate (Noll et al., 2018a). Our regression analysis also revealed that there might be seasonal variations of the time constant. The values of 2.6 ± 0.1 hr for austral autumn and 4.0 ± 0.1 hr for austral winter show the largest discrepancies.

The scaling factors of the two basis climatologies for all 298 lines are provided in the right column of Figure 4 (matrix **B** in Section 3.2) as a function of the energy of the upper state of the transition reduced by the lowest energy for the corresponding v' , that is, this energy difference (given in inverse centimeters) mainly depends on N' . Except for a few unreliable outliers, the scaling factors indicate a clear transition from climatologies with a slight dominance of the second component (decaying daytime population) in the evening for the lowest v' and N' to a contribution of the first component (tidal features) of almost 100% for the highest N' irrespective of v' . For low rotational energies, the different v' are well separated with larger gaps for lower vibrational excitations. In an intermediate zone between 500 and 1300 cm^{-1} , the factors of lower v' show larger changes, which then leads to the vanishing discrepancies for the highest N' . This distribution is very similar to the effective emission heights derived by Noll et al. (2022b) for the same line set as correlation coefficients of +0.93 and -0.92 for the first and second NMF component demonstrate. This excellent agreement supports the assumption that the mixing of the two basis climatologies strongly depends on the height distribution of the emission. Hence, the differences in the coefficients for the studied lines should mostly be caused by the strong height dependence of the time constant for the decay of the daytime population of atomic oxygen.

While only a relatively narrow altitude range seems to significantly contribute to the second NMF component, tidal features should be present at all altitudes. Hence, the strength of these structures might depend on the studied OH line. With the NMF decomposition of the climatologies into two components, this question cannot be answered. However, we can directly measure features in the climatologies for this purpose. As the contribution of the decaying atomic oxygen population can be neglected in the morning, the best suitable feature is the maximum in May (Figure 4a). For an estimate of the strength of this feature, we divided the relative intensity at 04:30 LT in May by the value for the grid point at the same LT in August. This choice is a compromise between high contrast, good nighttime coverage, and late time. The resulting intensity ratios are plotted in Figure 5. The most prominent structure of the distribution of the 298 data points is the maximum in the energy range from 400 to 800 cm^{-1} . Interestingly, the Q2DWs in 2017 and 2019 investigated by Noll et al. (2022b) showed the largest amplitudes in

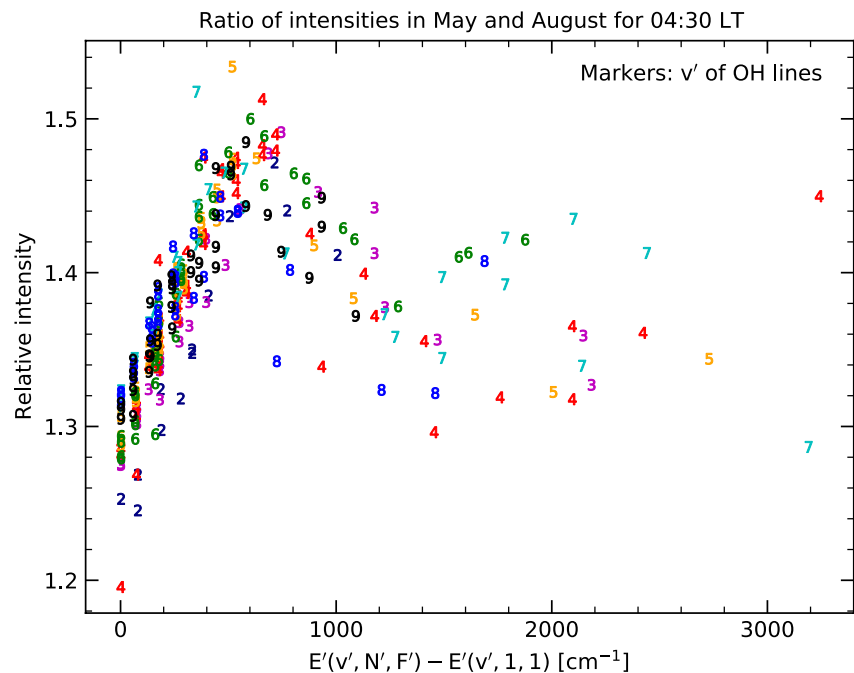


Figure 5. Ratio of intensities in May and August for 04:30 LT derived from the intensity climatologies of all 298 lines. The upper levels of the transitions are characterized by v' (markers) and the energy additional to the vibrational excitation (abscissa).

a similar range. As already stated in Section 1, this effect can be explained by an increased level of variability due to differences in the mixing of cold and hot populations caused by variations in the ambient temperature. It seems that variations by tides have a similar impact on OH emission. Nevertheless, the correlation coefficient for the whole set of lines in Figure 5 and the amplitude of the Q2DW event in 2017 is only +0.33. An important discrepancy is the lack of a dependence on v' for low N' . Moreover, the ratios for very high and low N' only differ by a few percent. Hence, structures that suggest an impact of the emission height cannot clearly be identified. The tidal modes that cause the measured climatological feature appear to affect the different emission altitudes at a similar time. The effective vertical wavelengths of these perturbations seem to be relatively long. This interpretation is supported by the fact that the location of the feature is relatively stable in the two example climatologies in Figure 2, which correspond to emissions with an effective altitude difference of about 5.5 km (Noll et al., 2022b). If this result was also valid for the other tidal features, the structures in the first NMF component could be similar for all OH lines.

4.2. Solar Cycle Effect

As already described in Section 3.1, we analyzed the impact of the solar cycle on OH intensities using a linear regression approach with the moving 27-day average S_{27d} of the solar radio flux at 10.7 cm as a proxy. Calculations with an additional linear long-term trend showed that the latter can be neglected. The ratio of the mean SCE without and with this trend for all 30 min bins of all OH lines did not significantly differ from unity (0.977). Moreover, the long-term trend was not significant ($+1.2 \pm 0.9\%$ per decade). These results confirm previous findings (Gao et al., 2016; Noll et al., 2017). Hence, the subsequent regression results were obtained with the solar radio flux as the only parameter. Our data set covers almost the entire solar cycle 24, that is, the time series starts and ends with low solar activity as Figure 1b shows. The minimum S_{27d} for the 30 min bins in both halves of the interval are 71 sfu in October 2009 and 67 sfu in March 2018. The maximum of 166 sfu was achieved in February 2014. Hence, the impact of solar cycle 24 can be investigated for a range of about 100 sfu. The mean value also amounts to about 100 sfu. The regression analysis was separately performed for the subsamples of each climatological grid point, which allowed us to study the influence of the solar activity cycle as a function of LT and month.

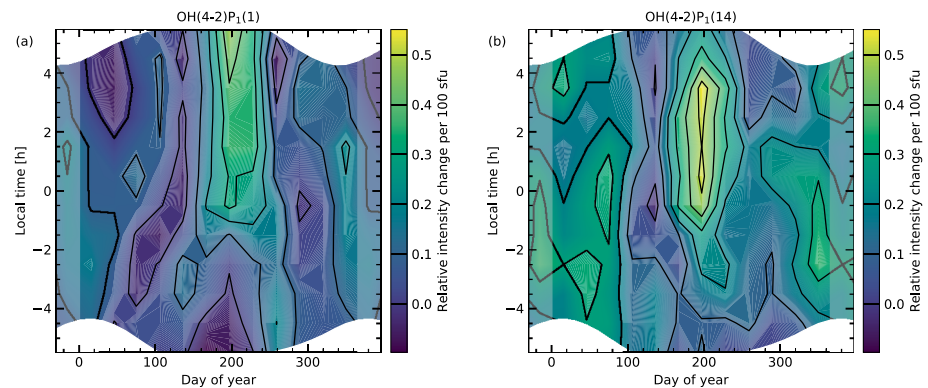


Figure 6. Climatologies of solar cycle effect relative to the intensity climatologies in Figure 2 (see caption for plot details) for OH(4-2) $P_1(1)$ (a) and OH(4-2) $P_1(14)$ (b). The climatologies indicate the response of OH emission to changes of the solar radio flux averaged for 27 days by 100 sfu. Each value of the climatological grid is given relative to the corresponding mean intensity.

The results for our two example lines relative to the corresponding intensity climatologies (Figure 2) and for a change of 100 sfu are shown in Figure 6. The climatologies are remarkable in terms of the large inhomogeneities of the SCE. A particularly strong influence of the solar activity on the OH intensities can be found from midnight to dawn around July. Then, a relative SCE of more than +40% (with uncertainties lower than 10%) per 100 sfu is possible. For the rest of the climatology, the response of the OH emission is usually much weaker. Even negative values cannot be excluded. Only around the turn of the year, the significance of the regression slopes for part of the grid points is sufficient to safely assume a positive effect. The major difference between the patterns for both lines is the location of the maximum with a width of several hours in austral winter. For OH(4-2) $P_1(14)$, it seems to be shifted by a few hours toward earlier LTs. An exact measurement is difficult as OH(4-2) $P_1(1)$ shows the highest value just before twilight. The latter line also indicates a weaker decrease of the SCE toward August than in the other case.

Climatologies of the OH-related SCE were rarely investigated before. Pertsev and Perminov (2008) compared the months November to January with the period from May to July for measurements of the OH(6-2) band in the years from 2000 to 2006 at Zvenigorod (56°N, 37°E) and found a factor of about 2. With an extension of this data set until 2018, Dalin et al. (2020) obtained a most likely ratio of 1.4 for the periods from 1 October to 31 March and from 20 May to 15 August. Taking OH(6-3) $P_1(3)$ for a comparison, we find for the ratio of the intervals from May to August and from October to March a value of 1.4, which is close to the results of Dalin et al. (2020) if we consider a shift in the seasons by 6 months due to the different hemisphere. The ratio drops to about 1.2 if April and September are also included in the austral winter period. The ratio depends on the selected lines. For our low and high N' examples in Figure 6, we obtain 1.7 and 0.8 for the two intervals with a length of 6 months. Gao et al. (2016) used global SABER OH data from January 2002 to January 2015 to derive the seasonal dependence of the SCE. The result is a maximum in March, which is about three times stronger than the minimum in December. Moreover, July apparently belongs to the months with the weakest SCE. These large discrepancies might be explained by the comparison of global to local results and the sparse LT coverage of the SABER data. For Cerro Paranal, it seems that the local times with the largest SCE in austral winter are not well covered (Noll et al., 2017). Finally, Reid et al. (2014) investigated the amplitude of the solar cycle in OH(8-3) emission at Buckland Park in Australia (see Section 4.1) for different LT intervals. The SCE appears to be strongest between 3:00 and 06:00 with a factor of about 1.3 compared to the minimum for 0:00 to 03:00. Using OH(8-5) $P_1(3)$ and the same LT binning, we find the maximum in the latter interval and about twice as strong as the minimum in the evening from 18:00 to 21:00. Hence, there is a different pattern, which might be related to the differences in the site, the time coverage (1995–2010), and the approach (harmonic analysis for multiple periods).

We also derived the effective SCE for each OH line. For this purpose, we averaged the relative values for the climatological grid cells under consideration of the corresponding nighttime contribution, that is, the fraction of the hour bin with a solar zenith angle greater than 100°. This approach minimizes the impact of inhomogeneities in the time series and the structure of the intensity climatologies. The results are shown in Figure 7a. Although there is some scatter by measurement uncertainties, which obviously have a larger impact on the related

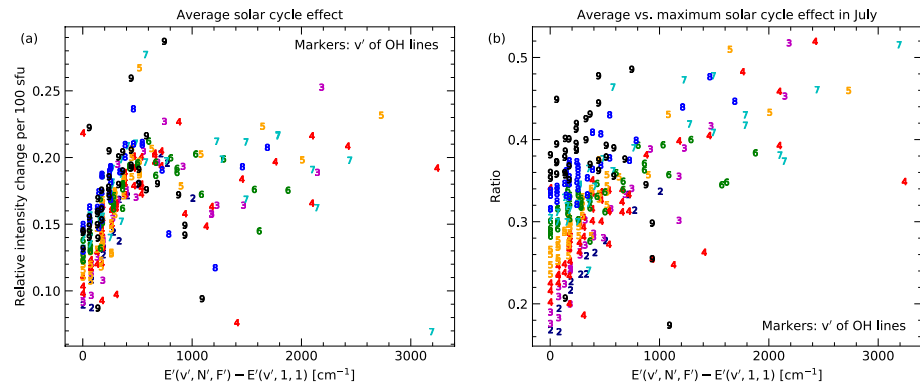


Figure 7. Average of solar cycle effect from the corresponding nighttime climatology (examples in Figure 6) for all 298 lines (a). The ratio of this average for the entire nocturnal year and the maximum in July is given in (b) for each line. The plotted line properties are discussed in the caption of Figure 4.

regression analysis than on the simple averaging of intensities, a clear trend is visible for rotational energies up to about 600 cm^{-1} . There, the average SCE increases with higher v' (at least up to 8) and N' . For higher energies, the effect seems to be relatively constant. Even a slight decrease is possible. The reliable data points are probably located in the range from 8% to 23% per 100 sfu. The strong dependence of the effective SCE on the OH line parameters was not seen before. Pertsev and Perminov (2008) stated that the SCEs for OH bands with v' between 3 and 9 were similar at Zvenigorod. Solar forcing for OH emission at Cerro Paranal was already investigated by Noll et al. (2017) based on optical spectra for the period from April 2000 to March 2015. The results were restricted to summed intensities of lines with low N' of bands with v' between 5 and 9. All bands showed relative SCEs of about 16% per 100 sfu with uncertainties much larger than the discrepancies. A mild trend could be possible for the two OH channels of SABER (Russell et al., 1999). Global data suggest a ratio of about 1.1 for the relative SCEs of the channels centered on 2.1 and 1.6 μm (Gao et al., 2016) with effective v' of 8.3 and 4.6, respectively (Noll et al., 2016). Noll et al. (2017) also presented SABER results for the region around Cerro Paranal. For the years from 2002 to 2015, the corresponding ratio derived from 14.5 ± 1.3 and $12.1 \pm 1.5\%$ per 100 sfu is 1.2 but with relatively high uncertainties. The obvious main reason for the lack of strong differences is the fact that only lines with low N' significantly contributed and the range of v' was limited. On the other hand, Figure 7a suggests that SCEs that were previously estimated are in good agreement with our results (despite the differences in the samples) if we focus on the relevant lines.

For a better understanding of the line dependence of the SCE, we also derived the maximum amplitude for each line in July, that is, the month with the strongest positive response. The results (not plotted but available via the data release) are very different from those of the effective SCE. With a range of the reliable values from 37% to 67% per 100 sfu, the maximum-to-minimum ratio is distinctly smaller than for the effective SCE. As the highest values are present in the energy range from 300 to 800 cm^{-1} , there is a clear similarity to the distribution for the intensity ratio plotted in Figure 5 and the amplitude of the Q2DWs studied by Noll et al. (2022b). Consequently, the maximum SCE also appears to be significantly affected by the mixing of cold and hot populations. Interestingly, the amplitude increases with decreasing v' for low N' , which is contrary to the effective SCE in Figure 7a but agrees with the results for the Q2DW in 2017. In the latter case, the corresponding correlation coefficient of +0.74 is therefore relatively high. The discrepancies between the effective and the maximum SCE are visualized in Figure 7b, which shows the ratio of both quantities for all OH lines. Starting with a minimum of about 0.17 for $v' = 2$ and $\Delta E'$ near 0 cm^{-1} , the ratio strongly increases for higher v' (up to 0.38 at 0 cm^{-1}) and higher N' (average of 0.43 for $\Delta E' > 1500 \text{ cm}^{-1}$). The bump related to the population mixing has obviously vanished, that is, the effective and maximum SCE appear to be affected by this feature in a similar way. The remaining probably monotonic increase with a flattening for the highest rotational energies is reminiscent of the distribution of the effective emission height of the investigated lines (Noll et al., 2022b). The correlation coefficient for the comparison of the mean-to-maximum ratio with these heights is +0.80 despite several outliers in Figure 7b. Hence, the ratio is mainly a function of the emission height. At least in part, this might be explained by the location of the maximum SCE with respect to LT as shown in Figure 6. While the range of increased SCE in July is well covered by the nighttime climatology of OH(4-2) $P_1(14)$, the largest values for OH(4-2) $P_1(1)$ are achieved before dawn. In the

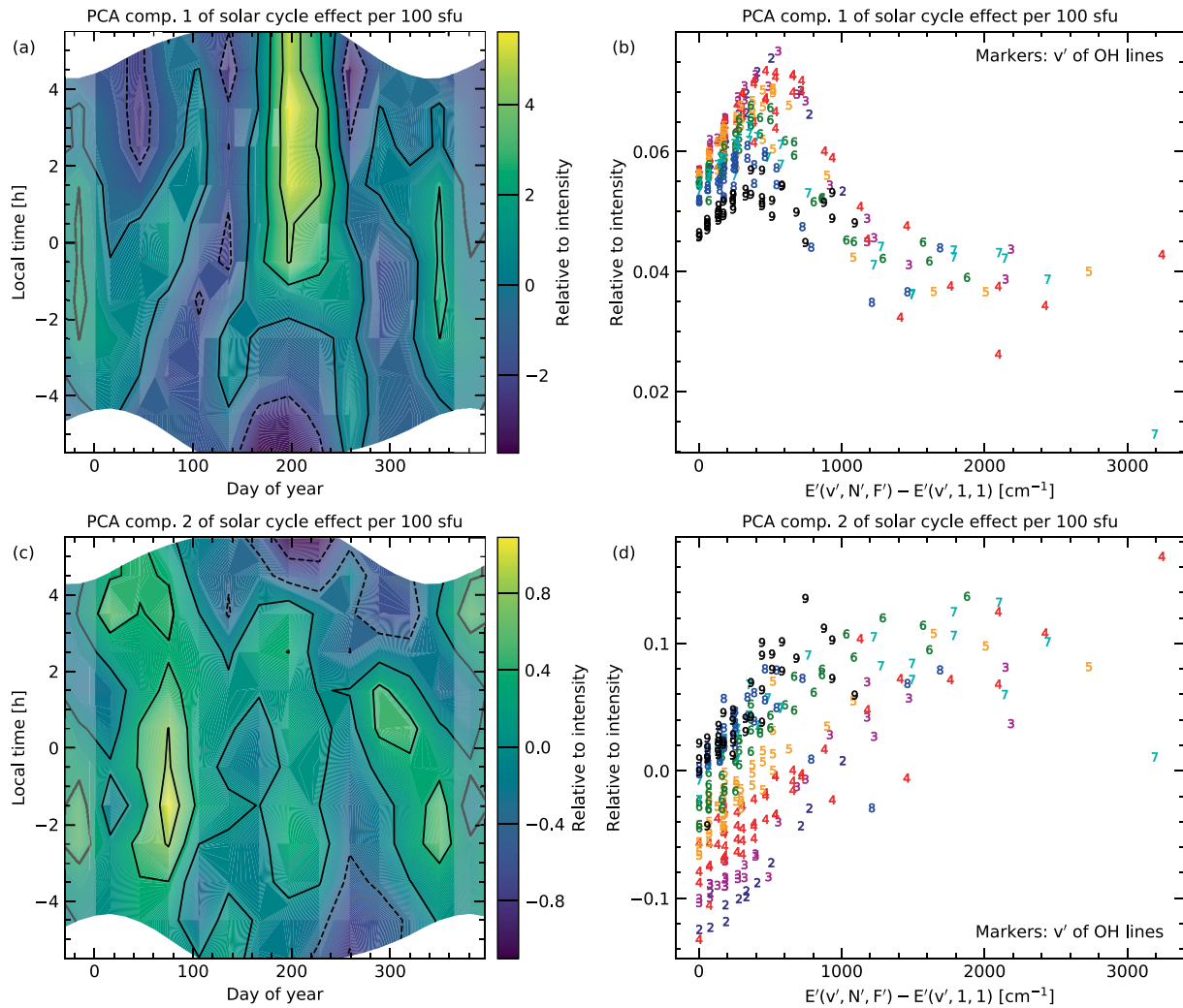


Figure 8. Decomposition of climatologies of solar cycle effect (examples in Figure 6) with principal component analysis for two components. The plots in the left and right column correspond to the content of matrices **T** and **W** described in Section 3.2. The plot details are similar to those of Figure 4.

latter case, the favorable conditions for a strong effect may extend to later LTs. Hence, the restriction to nighttime observations seems to cause an increasing loss of times with strong solar forcing for OH lines with lower effective emission heights, which then contributes to the observed wide spread of the effective SCEs.

An alternative approach for the analysis of the climatologies is the use of decomposition techniques as described in Section 3.2. As the SCE can also be negative, we prefer the PCA here. The results for the first two components, which explain 90.3% and 3.6% of the variance, are shown in Figure 8. The first basis climatology in (a) (first column of matrix **T** in Section 3.2) is an intermediate case compared to the patterns for the two example lines displayed in Figure 6. The corresponding scaling factors for the individual lines in (b) (first column of **W**) show a clear bump at intermediate rotational energies. Hence, this is another confirmation of the increased impact of temperature variations for OH rotational levels with similar contributions of cold and hot populations. The entire distribution of the data points is very similar to the one for the Q2DW in 2017 shown by Noll et al. (2022b). Benefiting from the noise-reducing properties of the PCA, the correlation coefficient is +0.96. It is remarkable that two phenomena which are related to time scales that differ by several orders of magnitude can produce such a similar response of the OH emission intensity. The second PCA component in (c) (second column of **T**) tends to show positive values in the middle of the night and exhibits the most negative values close to the morning twilight in July and August. Thus, positive scaling factors lead to a shift of the feature with the strongest SCE toward earlier LTs in the combined climatologies. The coefficients in (d) (second column of **W**) therefore represent a

measure of the shift in LT for each OH line. The data distribution supports our conclusion that the high SCEs in austral winter are present at later times for decreasing ν' and N' . Moreover, this distribution is highly correlated with the effective emission heights ($r = +0.89$), which demonstrates that the shift of the SCE features is primarily altitude dependent. As the representative LTs are earlier for higher altitudes, the SCE appears to be influenced by upward-propagating perturbations. As we investigate climatologies, the formation of a robust pattern is only imaginable in the case of tides. Hence, the impact of tides on the mesopause region appears to affect the sensitivity of OH emission to solar forcing. As the shifts could amount to several hours, the vertical wavelengths of the relevant tidal modes need to be relatively short. We will provide a more quantitative discussion of this topic in Section 4.3.2.

Changes in the solar activity affect the daytime production of atomic oxygen and hydrogen by photolysis as well as the energy input into the atmosphere indicated by the ambient temperature (e.g., Beig et al., 2008; Marsh et al., 2007). Both effects modify the OH intensity. The impact of the solar cycle on the temperature at OH emission altitudes can be tested separately via the ratio of the OH(3-1) $P_1(1)$ and OH(3-1) $P_1(2)$ intensities (see Section 4.1). The corresponding SCE climatology shows a very similar seasonal pattern as in the case of the intensity of individual lines. Although the lines have low ν' and N' , the maximum effect occurs shortly after midnight in austral winter, which better matches lines like OH(4-2) $P_1(14)$ (Figure 6). This result supports our explanation of the shifts of the SCE pattern in LT direction since the effective height for rotational temperature changes tends to be several kilometers higher than the effective height for intensity variations (e.g., Noll et al., 2022b; Swenson & Gardner, 1998). The temperature changes are weighted by the OH intensity profile, whereas the intensity changes usually maximize in the lower part of the layer due to the steepening of the atomic oxygen gradient (e.g., Smith et al., 2010). With respect to the presence of atomic oxygen at relatively low altitudes, the solar activity cycle seems to have a similar impact as waves with much shorter time scales.

4.3. Residual Variability

We also investigated the variability of OH line intensities which cannot be explained by the average climatologies discussed in Section 4.1 and those related to the SCE presented in Section 4.2. For this purpose, we calculated a line-specific model intensity for each 30 min bin depending on the LT interval, month, and the deviation of the solar radio flux S_{27d} from 100 sfu using the corresponding climatologies for relative intensity and SCE. The model values were then subtracted from the measured relative intensities. Climatologies of the residual variability can now be derived by the calculation of the standard deviation of the corrected relative intensities for the subsamples related to each climatological grid point (see Section 3.1). For our two example lines, the results are provided in the top row of Figure 9. Both climatologies show the highest values in June and July and a second maximum around January. The main discrepancy is the LT range with the highest residual variability relative to the climatological mean. The later maximum for OH(4-2) $P_1(1)$ qualitatively agrees with the results for the SCE (Figure 6).

As already discussed in Section 3.3, we analyzed the time dependence of the residual variability by means of the calculation of the sample variance for data pairs with the same time difference. With this approach, it was possible to derive climatologies for short-term variability with time scales shorter than a day and the amplitude of the Q2DW for each OH line. As we only needed to use the frequently occurring time differences of 24, 48, and 72 hr for the calculation of these properties, the results are relatively robust. We discuss them in the following.

4.3.1. Short-Term Variability

As demonstrated by Figure 3 for OH(4-2) $P_1(1)$, the variance in the corrected intensities is dominated by short time scales up to a few hours. Using the minimum of the variance values for 24 and 48 hr as a measure, the short-term variability corresponds to 75% of the total residual variance in the case of OH(4-2) $P_1(1)$ and 70% in the case of OH(4-2) $P_1(14)$. These percentages are the averages for the nighttime climatological grid. The individual grid points for OH(4-2) $P_1(1)$ reveal a clear seasonal variation with the highest and lowest fractions in austral winter (84% in August) and summer (61% in January), respectively. The absolute minimum of 47% at around 03:30 LT in January matches the summer maximum of the residual variability. As a consequence, the resulting short-term variability in Figure 9c only indicates one pronounced maximum in the second half of the night in June and July. The secondary maximum in January has mostly vanished. For the weak OH(4-2) $P_1(14)$ line, the variance fractions are relatively noisy. Nevertheless, relatively low variance ratios in the evening in summer lead to the

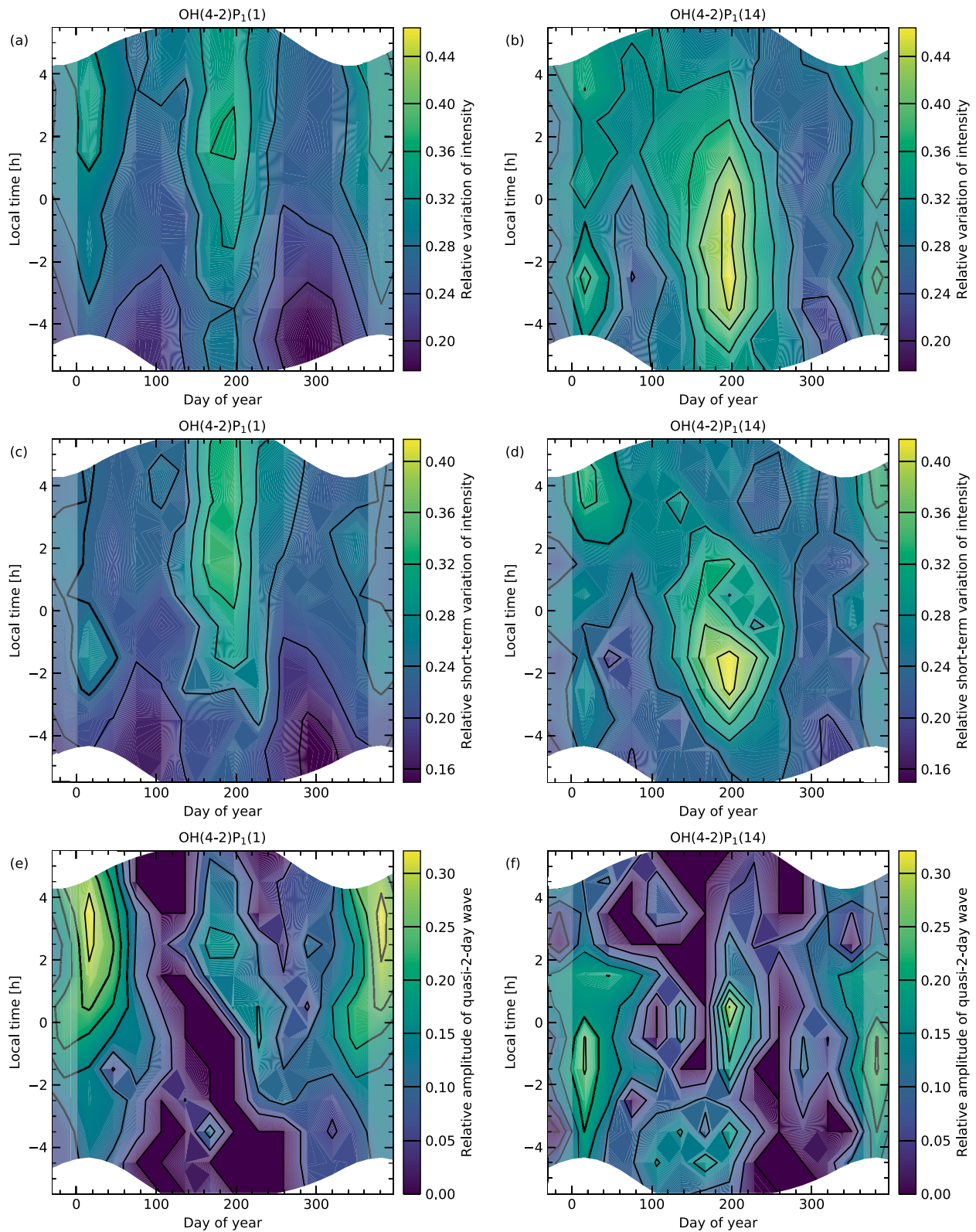


Figure 9. Climatologies of residual variability (standard deviation; top row), short-term variability (residual variations for time scales less than a day; middle row), and amplitude of quasi-2-day wave (bottom row) relative to the intensity climatologies in Figure 2 (see caption for plot details) for OH(4-2)P₁(1) (left column) and OH(4-2)P₁(14) (right column).

weakening of the summer peak in Figure 9d. Again, there is only one dominating climatological maximum in winter but earlier in the night compared to OH(4-2)P₁(1). The exact shape of this structure remains unclear due to the relatively high uncertainties with respect to the variance fraction.

Our results for the seasonal pattern can be compared to a study of the variance of the intensity of the OH(6-2) band measured at El Leoncito in the Argentinian Andes (32°S, 69°W) by Reisin and Scheer (2004). After the removal of diurnal and semidiurnal tidal modes by means of a fitting procedure, the authors also obtained a clear primary maximum in June and July, and a weaker secondary one in December and January. This pattern, which was explained by variations in the GW activity, is also present in the corresponding results for OH(6-2)-based rotational temperatures, which is consistent with our climatology for the ratio of OH(3-1)P₁(1) and OH(3-1)P₁(2) (see Section 4.1) that indicates a similar LT dependence of the winter maximum as in the case of the short-term intensity variance for the individual lines. In addition, significantly increased GW activity in austral winter was found by Alexander et al. (2015) in SABER temperature fluctuations with vertical wavelengths between 5 and 20 km for the region around the Andes between 29° and 36°S in the mesosphere and stratosphere, that is, at significantly lower altitudes than those related to the OH emission. SABER-based global maps of GW amplitude and momentum flux at 30 km (Ern et al., 2018; Preusse et al., 2009) also reveal a winter maximum at Cerro Paranal. The increased activity seems to be connected to the GW hot spot in the southern Andes, that is, the winter polar vortex and orographic forcing obviously play a role. According to the maps, the shallow summer maximum is probably related to GWs forced by deep convection, which have a hot spot east of the Andes at low southern latitudes in summer. At least for short-period waves with periods of 5–10 min, this interpretation seems to be supported by broad-band OH airglow imaging at Cerro Pachón in Chile (30°S, 71°W) studied by Cao and Liu (2022). The observations show preferential propagation directions toward the south (and also west) in austral summer and toward the north (and also east) in winter. Filtering effects (e.g., Fritts & Alexander, 2003) certainly contributed to this pattern as the wind measured by a meteor radar at the same site tended to indicate opposite directions, that is, critical similarities in speed and direction were reduced. According to Cao and Liu (2022), the majority of the detected waves was probably not directly propagating from the tropospheric hot spots. Either wave ducting in the mesopause region (e.g., Walterscheid et al., 1999) or secondary wave generation related to wave breaking at lower levels should be crucial. The importance of secondary waves is also discussed by other studies related to the same geographical region (Liu et al., 2019; Vadas et al., 2019; Vargas et al., 2016). As indicated by Figure 3, most of the measured variance is related to perturbations with periods of hours, that is, significantly longer than for the waves studied by Cao and Liu (2022). Long-period GWs tend to propagate mainly horizontally and can therefore be detected far from the source region for favorable atmospheric conditions (e.g., Fritts & Alexander, 2003). Hence, it is more likely to observe waves at Cerro Paranal that directly originate from the tropospheric source regions than in the case of short-period waves. Note that such discrepancies in the propagation properties can contribute to period-dependent differences in the seasonal wave activity (e.g., Sedlak et al., 2020).

In conclusion, the relatively strong short-term variations in the X-shooter OH data in June and July appear to be mainly produced by primary or secondary GWs related to the winter hot spot south of Cerro Paranal. Nevertheless, the details of the generation, propagation, and filtering of the relevant waves remain relatively uncertain. The OH intensity variance for time scales of hours may be affected by day-to-day changes in the tidal pattern. However, such changes can be forced by varying interactions with GWs (e.g., Fritts & Alexander, 2003; Smith, 2012), that is, the origin of the observed OH intensity variance would still be GWs. The scenario of strong interactions between tides and GWs seems to be supported by the fact that the enhanced climatological short-term variations in austral winter in Figure 9 are obviously embedded in the area of the intensity climatologies where the strongest tidal variations as indicated by Figure 4a are present. Moreover, there is an interesting similarity in the climatologies of the short-term variations and the SCE, which also shows the largest effects in the second half of the night in winter in the case of OH(4-2)P₁(1) (Figure 6a). Although the maximum SCE appears to be later in LT (a few hours) and day of year (a few weeks), the correlation coefficient for these well-defined features of similar shape is still 0.53. Hence, it could be that the increased SCE is related to enhanced GW activity. The stronger vertical transport by the wave-induced perturbations might increase the sensitivity of the OH production and emission to the atmospheric changes related to solar activity (such as the increased production of atomic oxygen).

In the following, we discuss the dependence of the short-term variations on the line parameters. Figure 10a shows the effective relative standard deviations for the entire nighttime climatologies. The plot was produced in the same way as for the SCE in Figure 7a. The distribution shows the typical features related to the mixing of cold

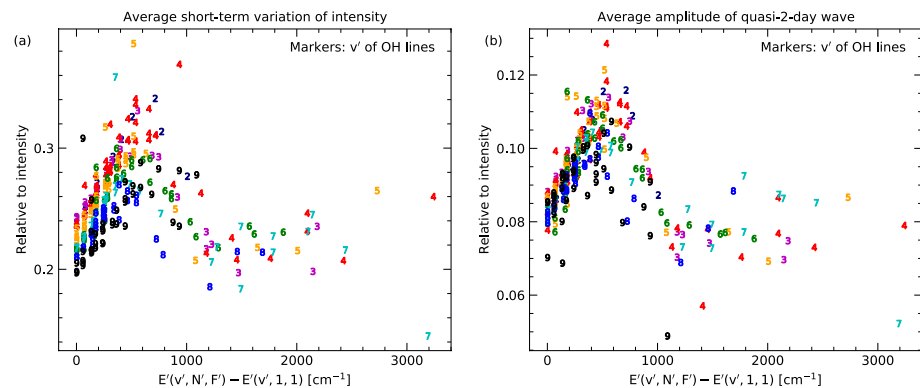


Figure 10. Average of short-term variability (a) and Q2DW amplitude (b) from the corresponding nighttime climatology (examples in Figure 9) for all 298 lines. The plotted line properties are discussed in the caption of Figure 4.

and hot rotational populations. Hence, there is a good positive correlation of $r = +0.77$ with the amplitude of the Q2DW from 2017 (Noll et al., 2022b). On the other hand, r is only $+0.28$ in the case of a comparison with the SCE-related Figure 7a. The discrepancies seem to be related to the location of the winter maximum in the climatologies. As discussed in Section 4.2, there appears to be a significant loss of high SCE values for OH levels with low v' and N' due to the morning twilight. This issue is less critical for the short-term variations, which show their highest values closer to midnight (e.g., Figures 6a and 9c). In agreement with this assumption, a high r of $+0.83$ is found if the short-term variations are only compared with the maximum SCE in July.

In Figure 11, we show the PCA results for the climatologies of the short-term variations. The first and the second component, which explain 83.6% and 5.3% of the variance, show similar structures as those for the SCE. The scaling factors of both components in the right panels of Figure 11 correlate with the corresponding ones for the SCE in Figure 8 with r of $+0.81$ and $+0.94$, respectively. The first value seems to be lowered by the relatively large spread with respect to the vibrational levels in Figure 11b. This also causes a relatively strong negative correlation with the effective emission heights of -0.80 (compared to $+0.85$ for the amplitude of the Q2DW in 2017). However, the second component still shows a distinctly stronger dependence on the emission height ($r = +0.89$) in agreement with the results for the SCE. Consequently, the PCA reveals that the line dependence of the short-term variations can also mainly be explained by a combination of an amplitude increase for intermediate N' due to an increased sensitivity to temperature variations (population mixing) and a height-dependent shift of the climatological pattern in LT direction. The latter is related to a basis climatology for the second component (Figure 11c) with an earlier decrease of the values in winter (in the middle of the night) than in the case of the SCE (around 04:00 LT, Figure 8c). If we explain the short-term variations as mainly caused by GWs as discussed before, these results imply that the presence of GW features in OH emission depends on LT and height. As the maximum range of effective emission heights for our line set is about 8 km on average (Noll et al., 2022b) with similar layer widths (e.g., Baker & Stair, 1988; Noll et al., 2016), possible changes in the GW sources and filtering effects below the mesopause region do not appear to be favorable explanations. Variations in the location of critical layers important for wave breaking and wave ducts may play a role. However, as already discussed in Section 4.1 with respect to the intensity climatologies, especially the vertical distribution of atomic oxygen can cause strong line-dependent differences. In this context, height-dependent variations of the concentration (accompanied by temperature changes) by independent perturbations seem to be important. Considering the amplification of waves with periods of integer fractions of a day in the climatologies and the shift of the pattern toward earlier LTs (up to several hours) with increasing height, rising solar tides could be crucial again. They appear to be able to alter the OH-related chemistry in a way that significantly affects the sensitivity of OH-based observations of GW activity.

4.3.2. Quasi-2-Day Wave

As described in Section 3.3, we can also derive 2D climatologies of the relative amplitude of the Q2DW based on the differences of the residual variances for time differences of 2 and 1 plus 3 days. Hence, we can extend the investigation of Q2DW activity in January/February 2017 (eight nights) and January 2019 (seven nights) (Noll et al., 2022b) by a more statistical approach for the entire data set. For our two example lines, the results are shown in the bottom row of Figure 9. The climatologies display clear maximum values in January at about

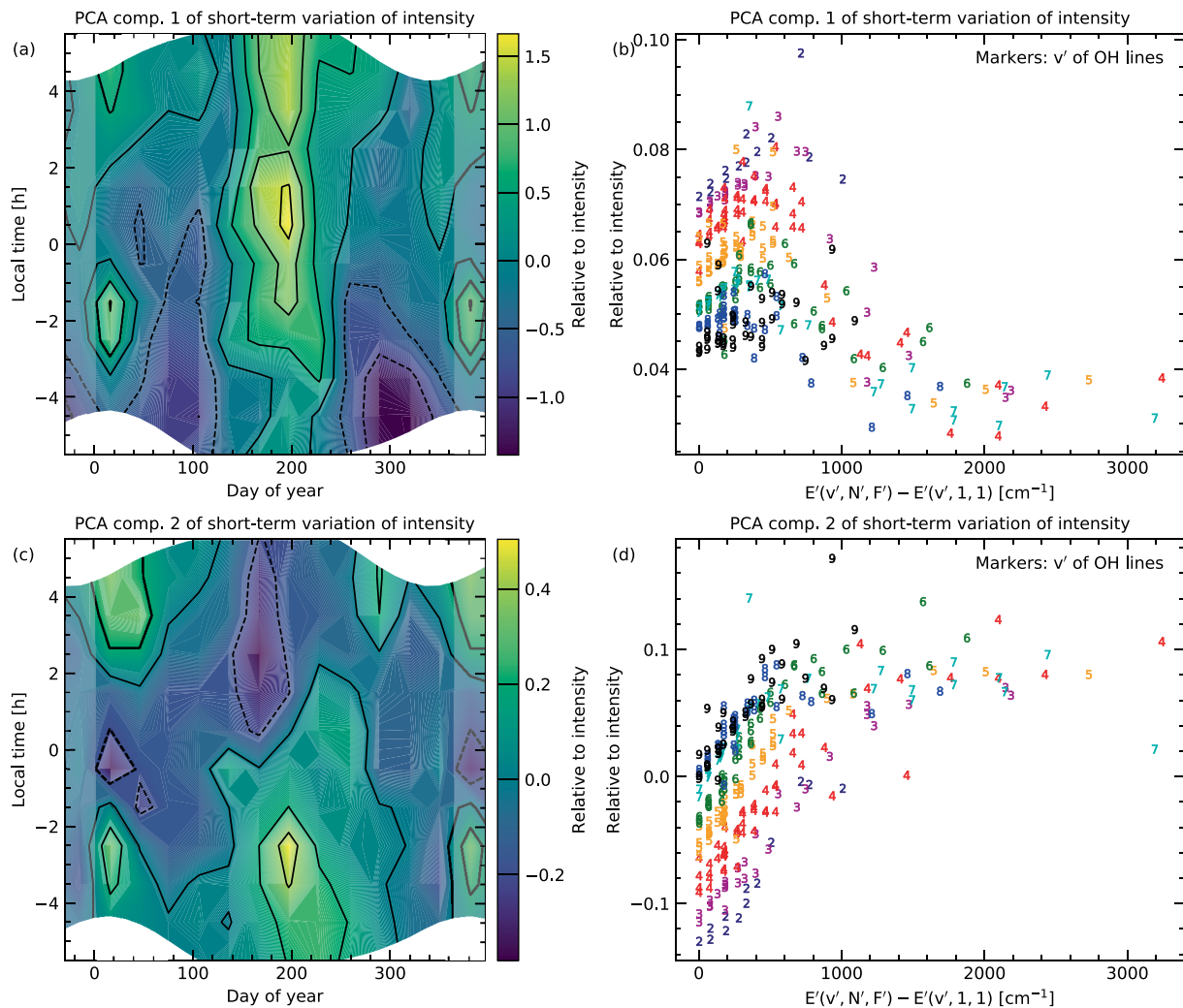


Figure 11. Decomposition of climatologies of short-term variability (examples in Figure 9) with principal component analysis for two components. The figure is similar to Figure 8.

03:00 LT for OH(4-2) P_1 (1) and about 23:00 LT for OH(4-2) P_1 (14), that is, they are separated by about 4 hr. In this month, the average Q2DW-related variance for both lines is almost on a similar level as the dominating short-term intensity variations discussed in Section 4.3.1 (ratios of 0.89 and 0.49 respectively). Hence, a significant fraction of the residual variability in January is obviously caused by Q2DW activity. The sharp peak at 00:30 LT in July for the relatively faint OH(4-2) P_1 (14) emission in (f) is probably caused by measurement uncertainties since such a strong feature at this position is not visible in the climatologies of other lines with high N' . Consequently, the less extended LT range with strong short-term variations in July in (d) compared to the pattern for the entire residual variability in (b) can also be explained by this issue. An outlier can occur more easily in (f) than in (b) of Figure 9 since the residual variances for the required specific time differences are based on smaller samples. In the case of 00:30 LT in July, there was only a particularly small number of only 101 data pairs for the calculation of the variance for $\Delta t = 72$ hr (cf. Section 3.3), whereas the sample of 30 min bins comprised 468 values for this grid point. Moreover, we estimated the uncertainties in the Q2DW amplitude using half the difference in the variance s^2 for $\Delta t = 24$ and 72 hr (ignoring possible true systematic differences) as the error for s^2 at 24, 48, and 72 hr, respectively. For those climatological grid points with an amplitude at least half as strong as the maximum in January, we then derived a satisfying mean relative uncertainty of about 18% for both lines in austral summer. On the other hand, the percentage is about 55% for OH(4-2) P_1 (14) in the rest of the year.

The location of the maximum values in January agrees well with the expected activity period of a westward-propagating Q2DW with a zonal wavenumber of 3 (e.g., Tunbridge et al., 2011). The later peak for

OH(4-2) $P_1(1)$ is consistent with the studies of specific time series by Noll et al. (2022b). Interestingly, the maximum values appear to be more pronounced and more clearly separated in the climatologies. The maximum relative amplitudes in (e) and (f) are 0.32 and 0.26, respectively. The corresponding values for the strong event in 2017 were 0.74 and 0.46. On the other hand, the moderate event in 2019 with only a weak LT dependence indicated 0.31 and 0.49, respectively. Our Q2DW climatologies should be more representative than the two short time intervals that were studied by Noll et al. (2022b). However, the gaps in the X-shooter data set and the strong year-to-year changes in the Q2DW properties (e.g., Ern et al., 2013; Gu et al., 2019; Tunbridge et al., 2011) imply that these climatologies are only rough approximations of the long-term averages. For an illustration of the uncertainties, we recalculated the climatologies without the well-covered strong Q2DW event in 2017. The results indicate a decrease of the average amplitude in January by 21% and 10% for the two example lines with $N' = 1$ and 14. The main decrease is related to the second half of the night, which showed the highest amplitudes in 2017. As a consequence, the morning peak for OH(4-2) $P_1(1)$ became more diffuse with two apparent maxima, whereas the summer pattern in the climatology of the high- N' line did not change much. Hence, the eight nights in 2017 had a clear impact on the Q2DW climatologies in austral summer by increased averages and more pronounced peaks.

Similar to the properties that were discussed in the previous sections, we derived effective Q2DW amplitudes from the nighttime climatologies of the whole line set. The results are shown in Figure 10b. As significant activity of the Q2DW is restricted to the austral summer, the typical amplitude relative to the intensity climatology is only of the order of 10%. Nevertheless, the dependence of the values on v' and N' resembles other plots of this kind. For example, the effective short-term variations in Figure 10a show a good correlation with $r = +0.77$ despite differences in the outlier distribution. Of course, it is also interesting to compare with the corresponding results for the maximum amplitude of the Q2DW in 2017. Considering that there are large differences in the related samples (10 years vs. eight nights), the correlation coefficient of $r = +0.81$ indicates a convincing agreement. Moreover, the clear presence of the bump at intermediate N' supports the conclusion that the mixing of cold and hot populations seems to be a general driver for line-specific differences in the strengths of perturbations on various time scales.

In Figure 12, we show the results for the PCA of the climatologies of the Q2DW amplitude of all 298 lines. As in the case of the SCE and the short-term variations, we discuss the first two components, which explain 83.5% and 5.0% of the variance. The primary basis climatology in (a) indicates the expected strong maximum in the second half of the night in austral summer. Based on the full line set, the derived pattern can show possible features more clearly than the individual climatologies. Hence, there might be a weak secondary maximum in the same LT range in winter, which would not contradict other observations (e.g., Ern et al., 2013). The corresponding scaling factors in (b) confirm the typical amplitude distribution related to population mixing. With a correlation coefficient of +0.95, the pattern is very similar to the distribution of the amplitudes for the Q2DW event in 2017. Apart from comparing the same wave type, the noise-reducing property of the PCA certainly contributes to this very high r . In the same way as for the SCE and the short-term variations, the second basis climatology in (c) changes the LTs of the maximum activity. Positive scaling factors in (d) lead to a shift to earlier LTs. Again, these changes are strongly correlated with the effective emission height ($r = +0.94$). Hence, Q2DWs also appear to strongly interact with upward-propagating tides, which confirms the conclusions of Noll et al. (2022b) based on the LT dependence of the amplitude of the Q2DW from 2017. Interactions with migrating solar tides were already reported in previous studies (e.g., Hecht et al., 2010; Palo et al., 1999).

The well-localized peaks of the Q2DW amplitude in the individual climatologies as shown in the bottom panels in Figure 9 allow us to quantitatively analyze the relation of height and LT in order to learn more about the tidal modes that cause the observed activity shifts. For this purpose, we derived the LT bin in January with the maximum amplitude for the 298 studied OH lines and then averaged the reference emission heights from Noll et al. (2022b) for all lines with the maximum in a given bin. Thereafter, we performed a linear regression analysis of the average heights and the central times of the LT bins with a length of 1 hr. The relation between height and LT turned out to be almost perfectly linear with $r = -0.994$. The slope of the relation could therefore be derived with high accuracy, amounting to -1.23 ± 0.07 km hr⁻¹. This negative phase propagation can be converted into the vertical wavelength of a rising wave if the wave period is set. For a diurnal tide with a period of 24 hr, the result is 29.5 ± 1.6 km, which is remarkably close to the expected wavelength of the first symmetric westward propagating mode with a zonal wavenumber of 1. Forbes (1995) provide 27.9 km based on calculations. This migrating solar tide, which is also known as DW1, is the dominating tidal mode at low latitudes (e.g., Smith, 2012). The most important semidiurnal mode, the westward-migrating SW2 tide with a zonal wavenumber of 2 would need a

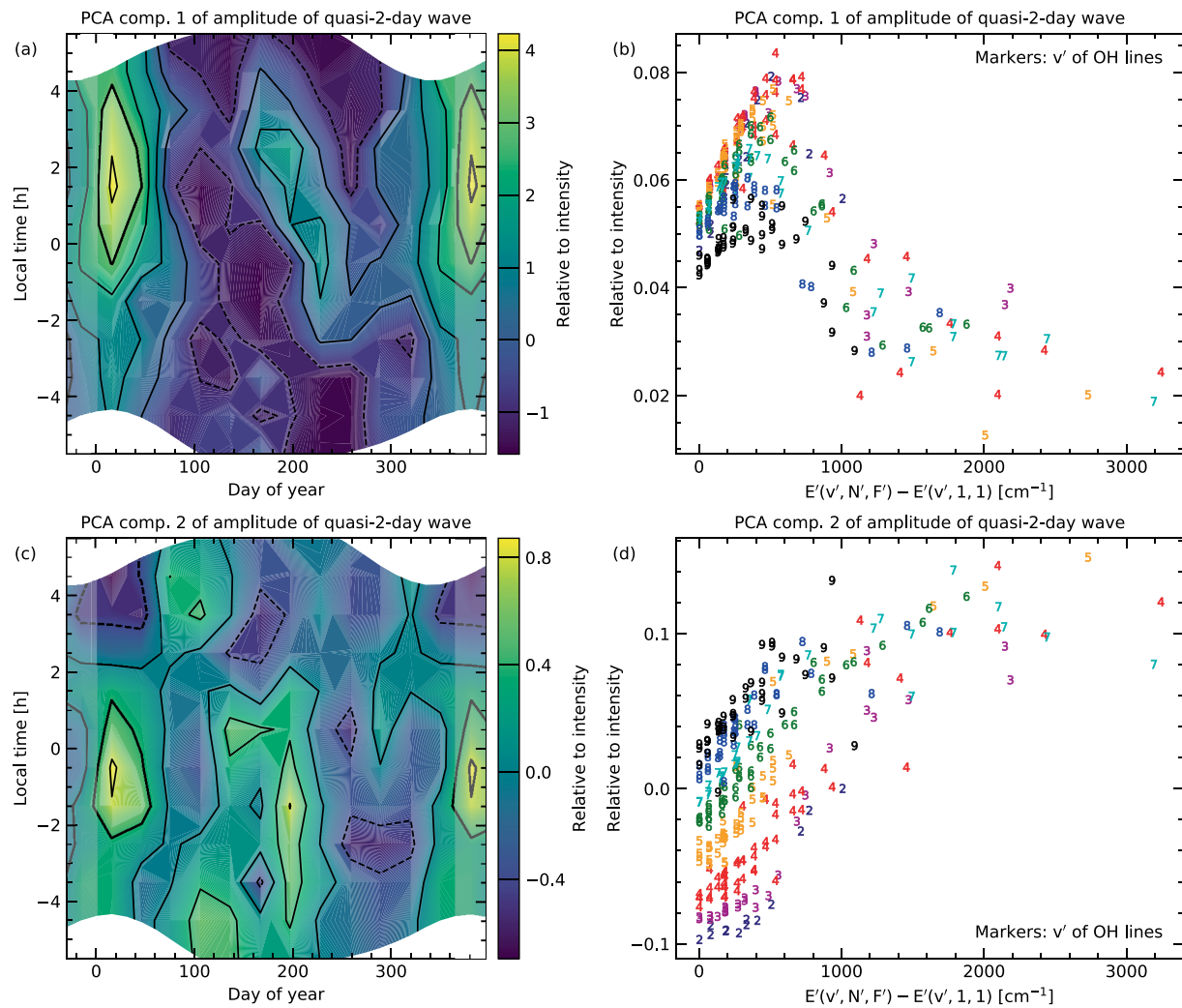


Figure 12. Decomposition of climatologies for Q2DW amplitude (examples in Figure 9) with principal component analysis for two components. The figure is similar to Figure 8.

wavelength of about 15 km in order to fit. However, its wavelength is clearly longer than in the case of the DW1 (Smith, 2012). Hence, it is likely that the line-dependent LT shift of the maximum Q2DW activity in January can mostly be explained by the interaction of Q2DW and DW1. The significant contribution of the Q2DW in 2017 to the climatologies seems to be important for this result since the LT difference for the two example lines as reported above would otherwise be more uncertain. The Q2DW in 2017 had a most probable wavelength of about 32 km during the analyzed eight nights (Noll et al., 2022b). As this is comparable to the DW1, strong interactions are likely. This statement is supported by the fact that the Q2DW from 2019, which did not show a strong LT dependence, had a very long vertical wavelength.

The interpretation of the line-dependent shifts of the patterns in the climatologies of the SCE and short-term variations is more difficult as the most striking features are broader and are partly cut by the nighttime limits. Nevertheless, there are clear indications that the situation for the Q2DW in austral summer can be generalized. The best examples are probably the climatologies of the residual variability for the two reference lines in the top row of Figure 9. These climatologies include the Q2DW as well as the GW activity. In these cases, the variability in January and July show a similar dependence on LT, at least with respect to the main peaks. The LT difference for the maximum in July is probably about 4 hr with an uncertainty of 1 hr, that is, very similar to the result for the Q2DW in January shown in the bottom panels. The extracted short-term variations in panels (c) and (d) of Figure 9 are also consistent with this estimate. In the case of the SCE shown in Figure 6, the interpretation is most

difficult but the minimum difference should be 2–3 hr. Hence, the DW1 is also the most likely tidal mode for the origin of the line-dependent changes in the climatological patterns of the short-term variations (i.e., especially GW activity) and the SCE. Nevertheless, the OH intensity variations are also affected by other tidal modes (with longer vertical wavelengths) as the analysis of the intensity climatologies in Section 4.1 indicates. There, the location of the tidal features appears to be relatively robust with respect to the line parameters.

5. Conclusions

We studied intensity time series (binned in 30 min steps) of 298 OH lines with respect to climatological variability patterns based on almost 90,000 near-infrared spectra taken at Cerro Paranal in Chile in the time interval from October 2009 to September 2019. Different 2D climatologies were calculated for LT and day of year with grid steps and (minimum) data selection radii of 1 hr and 1 month, respectively.

The climatologies of the OH intensities relative to the mean revealed a strong dependence on line parameters such as the upper vibrational level v' and upper rotational level N' . Using nonnegative matrix factorization for the decomposition of the observed patterns, we could clearly separate two major components. First, there is a relatively stable variability structure which can be explained by tidal features, which are strongest in the middle of the year. Similar features can also be observed in the temperature and atomic oxygen concentration at the altitudes with the strongest OH emission. Their amplitude seems to maximize for intermediate rotational energies between 400 and 800 cm^{-1} . A similar amplitude distribution was previously discovered by Noll et al. (2022b) for a Q2DW which was investigated in a time interval of eight nights in 2017 based on the same X-shooter data set. Another Q2DW in 2019 (seven nights) also showed this feature. It can obviously be explained by assuming that the population distribution for each v' can be described by the combination of a cold thermalized population with the effective ambient temperature at the OH emission heights and a hot nonthermalized population with v' -dependent pseudo temperatures (Noll et al., 2020). The maximum tidal variations are then found where both populations show similar contributions on average since the steep decrease of the cold population with increasing N' there causes a particular high variability of the population mixing if the ambient temperature changes. The second component of the relative intensity climatologies is characterized by a general decrease from the evening to the morning with amplitude maxima near the equinoxes. Assuming an exponential function, the effective time constant of the decrease is 3.3 ± 0.2 hr with possible seasonal variations. The contribution to the combined climatologies strongly decreases with increasing v' and N' and vanishes almost completely for the highest rotational levels. This behavior resulted in a strong anticorrelation with the effective line emission heights based on phase measurements in the X-shooter and related height-resolved SABER data for the Q2DW event in 2017 (Noll et al., 2022b). Supported by the results of Marsh et al. (2006), this component can be explained by the particularly strong decay of the nighttime population of atomic oxygen, which is essential for the OH production and is mostly produced by photolysis of molecular oxygen at daytime, at the lowest OH emission altitudes below 84 km.

We also calculated climatologies of the SCE relative to the corresponding intensity climatologies for 27-day averages of the solar radio flux. The effective SCE values derived from the entire nighttime climatologies show a large range between about 8% and 23% per 100 solar flux units (sfu), which was not observed before but is consistent with previous results if it is considered which OH lines contributed to the analysis. The lowest SCE values were found for the lines with the lowest v' and N' . Between intermediate and high rotational energies, no clear trend was seen. This distribution can be explained by the striking structure of the SCE climatologies with values between slightly negative and more than +50% per 100 sfu and its change depending on the line parameters. A PCA revealed that the primary component is characterized by a strongly positive effect in the second part of the night around July and only weak effects otherwise. This component also shows the highest values for intermediate N' , that is, differences in the sensitivity of the OH level populations to changes in the ambient temperature is the main reason for the observed discrepancies. The second component essentially describes a shift of this pattern in LT direction. As indicated by a very high correlation coefficient of +0.96, the LT of the maximum is later for lines with lower effective emission height. This effect obviously contributes to the low effective nighttime SCEs for lines with low v' and N' as the extension of the maximum feature in LT direction appears to be reduced by the end of the night. The shift of the SCE pattern can be best understood in terms of the impact of upward-propagating perturbations, which seem to change the sensitivity of the OH emission to atmospheric effects of solar activity such as higher atomic oxygen production and higher temperatures. As we investigate climatologies, the perturbations are most likely related to solar tides.

By correcting the OH intensity data for the mean climatologies and the SCE using the corresponding solar radio flux, we could also study climatologies of the residual variability consisting of the standard deviations for the selected subsamples for each climatological grid point. The results show maximum values around the solstices. With the derivation of the mean variance as a function of the time difference of data pairs for each subsample, we were able to distinguish between different variability sources. Time scales up to several hours are most important. Such short-term variations show a clear maximum in June and July, which is probably related to GWs that tended to be generated in the south toward the Andean winter hot spot and reached Cerro Paranal by favorable propagation conditions either directly, via wave ducts, or as secondary waves. These waves may also play an important role for the strong SCE effect that is present in a similar region of the climatologies. With respect to the activity maximum in austral winter, short-term variations only explain a part of the residual variability as especially January is characterized by a significant contribution of Q2DWs, which we also measured. The remaining activity on short time scales might mainly be related to GWs that originate from deep convection in the north and east on the other side of the Andes. For the climatologies of the short-term variations and the Q2DW amplitude, we also calculated effective values for each OH line. Compared to the SCE, they are less affected by the nighttime limitations as the LTs with the highest activity were not close to the twilight for all lines. As a consequence, the line-dependent distributions of both properties showed a clearer bump at intermediate N' . As the first PCA components also revealed this feature, it seems that the line-dependent mixing of cold and hot populations has a major impact on the amplitude of various kinds of variations with time scales that can differ by several orders of magnitude. Similar to the SCE, the second PCA components indicate clear shifts of the climatological patterns in LT direction that are strongly correlated with the effective emission heights of the lines. Hence, the impact of tides on the sensitivity of OH emission to perturbations can also be generalized. In order to learn more about the relevant tidal modes, we used the well-defined LTs of the maximum Q2DW amplitude in January (with clear impact of the strong event in 2017) of all 298 lines in order to link them to the corresponding effective emission heights. The resulting height–LT relation is almost perfectly linear with a slope of $-1.23 \pm 0.07 \text{ km hr}^{-1}$ that can be best explained by a wave period of 24 hr and a vertical wavelength of about 30 km. As the climatologies for short-term variations and SCE show similar pattern shifts, it appears that OH-based studies of GWs, Q2DWs, solar activity, and possibly other variability sources at Cerro Paranal and similar locations are significantly affected by the westward-propagating diurnal tide with zonal wavenumber 1, DW1. This tidal mode can act by direct interactions with the other perturbations and/or indirectly via the change of the OH-related chemistry, which particularly depends on the atomic oxygen profile.

Data Availability Statement

The basic X-shooter NIR-arm data for this project originate from the ESO Science Archive Facility at <http://archive.eso.org> (open access for all data used) and are related to various observing programs that were carried out between October 2009 and September 2019. The raw spectra were processed (using the corresponding calibration data) and then analyzed. Data of the analysis of eight nights in 2017 and seven nights in 2019 with respect to specific Q2DWs were already published (Noll et al., 2022a). We used the resulting line-dependent wave amplitudes and effective emission heights. Concerning this study, the line-specific time series (binned in 30 min steps) for the calculation of the climatologies and the results of the analysis as partly shown in the figures can be obtained from the public repository Zenodo at <http://zenodo.org/record/7826060> (Noll et al., 2023).

Acknowledgments

Stefan Noll is financed by the project NO 1328/1-3 of the German Research Foundation (DFG). The authors thank Sabine Möhler from ESO for her support with respect to the X-shooter calibration data. Moreover, the authors are grateful to the two anonymous reviewers for their valuable comments. Open Access funding enabled and organized by Projekt DEAL.

References

- Adler-Golden, S. (1997). Kinetic parameters for OH nightglow modeling consistent with recent laboratory measurements. *Journal of Geophysical Research*, 102(A9), 19969–19976. <https://doi.org/10.1029/97JA01622>
- Alexander, P., Torre, A., Schmidt, T., Llamedo, P., & Hierro, R. (2015). Limb sounders tracking topographic gravity wave activity from the stratosphere to the ionosphere around midlatitude Andes. *Journal of Geophysical Research: Space Physics*, 120(10), 9014–9022. <https://doi.org/10.1002/2015JA021409>
- Baker, D. J., & Stair, A. T., Jr. (1988). Rocket measurements of the altitude distributions of the hydroxyl airglow. *Physica Scripta*, 37(4), 611–622. <https://doi.org/10.1088/0031-8949/37/4/021>
- Bates, D. R., & Nicolet, M. (1950). The photochemistry of atmospheric water vapor. *Journal of Geophysical Research*, 55(3), 301–327. <https://doi.org/10.1029/JZ055i003p00301>
- Beig, G., Scheer, J., Mlynczak, M. G., & Keckhut, P. (2008). Overview of the temperature response in the mesosphere and lower thermosphere to solar activity. *Reviews of Geophysics*, 46(3), RG3002. <https://doi.org/10.1029/2007RG000236>
- Brooke, J. S. A., Bernath, P. F., Western, C. M., Sneden, C., Afşar, M., Li, G., & Gordon, I. E. (2016). Line strengths of rovibrational and rotational transitions in the X2Π ground state of OH. *Journal of Quantitative Spectroscopy and Radiative Transfer*, 168, 142–157. <https://doi.org/10.1016/j.jqsrt.2015.07.021>

- Cao, B., & Liu, A. Z. (2022). Statistical characteristics of high-frequency gravity waves observed by an airglow imager at Andes Lidar Observatory. *Earth and Space Science*, 9(6), e2022EA002256. <https://doi.org/10.1029/2022EA002256>
- Clough, S. A., Shephard, M. W., Mlawer, E. J., Delamere, J. S., Iacono, M. J., Cady-Pereira, K., et al. (2005). Atmospheric radiative transfer modeling: A summary of the AER codes. *Journal of Quantitative Spectroscopy and Radiative Transfer*, 91(2), 233–244. <https://doi.org/10.1016/j.jqsrt.2004.05.058>
- Cosby, P. C., & Slanger, T. G. (2007). OH spectroscopy and chemistry investigated with astronomical sky spectra. *Canadian Journal of Physics*, 85(2), 77–99. <https://doi.org/10.1139/P06-088>
- Dalin, P., Perminov, V., Pertsev, N., & Romejko, V. (2020). Updated long-term trends in mesopause temperature, airglow emissions, and noctilucent clouds. *Journal of Geophysical Research: Atmospheres*, 125(5), e30814. <https://doi.org/10.1029/2019JD030814>
- Dodd, J. A., Armstrong, P. S., Lipson, S. J., Lowell, J. R., Blumberg, W. A. M., Nadile, R. M., et al. (1994). Analysis of hydroxyl earthlimb airglow emissions: Kinetic model for state-to-state dynamics of OH(v,N). *Journal of Geophysical Research*, 99(D2), 3559–3586. <https://doi.org/10.1029/93JD03338>
- Ern, M., Preusse, P., Kalisch, S., Kaufmann, M., & Riese, M. (2013). Role of gravity waves in the forcing of quasi two-day waves in the mesosphere: An observational study. *Journal of Geophysical Research: Atmospheres*, 118(9), 3467–3485. <https://doi.org/10.1029/2012JD018208>
- Ern, M., Trinh, Q. T., Preusse, P., Gille, J. C., Mlynarczyk, M. G., Russell, I., et al. (2018). GRACILE: A comprehensive climatology of atmospheric gravity wave parameters based on satellite limb soundings. *Earth System Science Data*, 10(2), 857–892. <https://doi.org/10.5194/essd-10-857-2018>
- Forbes, J. M. (1995). Tidal and planetary waves. *Geophysical Monograph Series*, 87, 67–87. <https://doi.org/10.1029/GM087p0067>
- Fritts, D. C., & Alexander, M. J. (2003). Gravity wave dynamics and effects in the middle atmosphere. *Reviews of Geophysics*, 41(1), 1003. <https://doi.org/10.1029/2001RG000106>
- Gao, H., Xu, J., & Chen, G.-M. (2016). The responses of the nightglow emissions observed by the TIMED/SABER satellite to solar radiation. *Journal of Geophysical Research: Space Physics*, 121(2), 1627–1642. <https://doi.org/10.1002/2015JA021624>
- Gao, H., Xu, J., & Wu, Q. (2010). Seasonal and QBO variations in the OH nightglow emission observed by TIMED/SABER. *Journal of Geophysical Research*, 115(A6), A06313. <https://doi.org/10.1029/2009JA014641>
- Gu, S.-Y., Dou, X.-K., Yang, C.-Y., Jia, M., Huang, K.-M., Huang, C.-M., & Zhang, S.-D. (2019). Climatology and anomaly of the quasi-two-day wave behaviors during 2003-2018 austral summer periods. *Journal of Geophysical Research: Space Physics*, 124(1), 544–556. <https://doi.org/10.1029/2018JA026047>
- Hagan, M. E., Forbes, J. M., & Vial, F. (1995). On modeling migrating solar tides. *Geophysical Research Letters*, 22(8), 893–896. <https://doi.org/10.1029/95GL00783>
- Hannawald, P., Schmidt, C., Sedlak, R., Wüst, S., & Bittner, M. (2019). Seasonal and intra-diurnal variability of small-scale gravity waves in OH airglow at two Alpine stations. *Atmospheric Measurement Techniques*, 12(1), 457–469. <https://doi.org/10.5194/amt-12-457-2019>
- Hart, M. (2019). Long-term spectroscopic observations of the atmospheric airglow by the Sloan Digital Sky Survey. *Publications of the Astronomical Society of the Pacific*, 131(995), 015003. <https://doi.org/10.1088/1538-3873/aae972>
- Hecht, J. H., Walterscheid, R. L., Gelinis, L. J., Vincent, R. A., Reid, I. M., & Woithe, J. M. (2010). Observations of the phase-locked 2 day wave over the Australian sector using medium-frequency radar and airglow data. *Journal of Geophysical Research*, 115(D16), D16115. <https://doi.org/10.1029/2009JD013772>
- Holzlohner, R., Kimeswenger, S., Kausch, W., & Noll, S. (2021). Bolometric night sky temperature and subcooling of telescope structures. *Astronomy & Astrophysics*, 645, A32. <https://doi.org/10.1051/0004-6361/202038853>
- Kalogerakis, K. S., Matsiev, D., Cosby, P. C., Dodd, J. A., Falcinelli, S., Hedin, J., et al. (2018). New insights for mesospheric OH: Multi-quantum vibrational relaxation as a driver for non-local thermodynamic equilibrium. *Annals of Geophysics*, 36(1), 13–24. <https://doi.org/10.5194/angeo-36-13-2018>
- Kerber, F., Querel, R. R., Neureiter, B., & Hanuschik, R. (2016). Through thick and thin: Quantitative classification of photometric observing conditions on Paranal. In A. B. Peck, R. L. Seaman, & C. R. Benn (Eds.), *Observatory operations: Strategies, processes, and systems VI* (Vol. 9910, p. 99101S). <https://doi.org/10.1117/12.2232333>
- Kerber, F., Rose, T., Chacón, A., Cuevas, O., Czekala, H., Hanuschik, R., et al. (2012). A water vapour monitor at Paranal Observatory. In I. S. McLean, S. K. Ramsay, & H. Takami (Eds.), *Ground-based and airborne instrumentation for astronomy IV* (Vol. 8446, p. 84463N). <https://doi.org/10.1117/12.924340>
- Kim, Y. H., Lee, C., Chung, J.-K., Kim, J.-H., & Chun, H.-Y. (2010). Seasonal variations of mesospheric gravity waves observed with an airglow all-sky camera at Mt. Bohyun, Korea (36°N). *Journal of Astronomy and Space Sciences*, 27(3), 181–188. <https://doi.org/10.5140/JASS.2010.27.3.181>
- Lee, D. D., & Seung, H. S. (1999). Learning the parts of objects by non-negative matrix factorization. *Nature*, 401(6755), 788–791. <https://doi.org/10.1038/44565>
- Liu, X., Xu, J., Yue, J., Vadas, S. L., & Becker, E. (2019). Orographic primary and secondary gravity waves in the middle atmosphere from 16-year SABER observations. *Geophysical Research Letters*, 46(8), 4512–4522. <https://doi.org/10.1029/2019GL082256>
- López-González, M. J., García-Comas, M., Rodríguez, E., López-Puertas, M., Olivares, I., Jerónimo-Zafra, J. M., et al. (2020). Gravity wave activity in the middle atmosphere from SATI airglow observations at northern mid-latitude: Seasonal variation and comparison with tidal and planetary wave-like activity. *Journal of Atmospheric and Solar-Terrestrial Physics*, 206, 105329. <https://doi.org/10.1016/j.jastp.2020.105329>
- López-González, M. J., Rodríguez, E., García-Comas, M., Costa, V., Shepherd, M. G., Shepherd, G. G., et al. (2009). Climatology of planetary wave type oscillations with periods of 2-20 days derived from O₂ atmospheric and OH(6-2) airglow observations at mid-latitude with SATI. *Annals of Geophysics*, 27(9), 3645–3662. <https://doi.org/10.5194/angeo-27-3645-2009>
- Marsh, D. R., Garcia, R. R., Kinnison, D. E., Boville, B. A., Sassi, F., Solomon, S. C., & Matthes, K. (2007). Modeling the whole atmosphere response to solar cycle changes in radiative and geomagnetic forcing. *Journal of Geophysical Research*, 112(D23), D23306. <https://doi.org/10.1029/2006JD008306>
- Marsh, D. R., Smith, A. K., Mlynarczyk, M. G., & Russell, J. M., III. (2006). SABER observations of the OH Meinel airglow variability near the mesopause. *Journal of Geophysical Research*, 111(A10), A10S05. <https://doi.org/10.1029/2005JA011451>
- Modigliani, A., Goldoni, P., Royer, F., Haigron, R., Guglielmi, L., François, P., et al. (2010). The X-shooter pipeline. In D. R. Silva, A. B. Peck, & B. T. Soifer (Eds.), *Observatory operations: Strategies, processes, and systems III* (Vol. 7737, p. 773728). <https://doi.org/10.1117/12.857211>
- Moehler, S., Modigliani, A., Freudling, W., Giannichele, N., Gianninas, A., Gonneau, A., et al. (2014). Flux calibration of medium-resolution spectra from 300 nm to 2500 nm: Model reference spectra and telluric correction. *Astronomy & Astrophysics*, 568, A9. <https://doi.org/10.1051/0004-6361/201423790>
- Noll, S., Kausch, W., Barden, M., Jones, A. M., Szyzka, C., Kimeswenger, S., & Vinther, J. (2012). An atmospheric radiation model for Cerro Paranal. I. The optical spectral range. *Astronomy & Astrophysics*, 543, A92. <https://doi.org/10.1051/0004-6361/201219040>

- Noll, S., Kausch, W., Kimeswenger, S., Unterguggenberger, S., & Jones, A. M. (2015). OH populations and temperatures from simultaneous spectroscopic observations of 25 bands. *Atmospheric Chemistry and Physics*, *15*(7), 3647–3669. <https://doi.org/10.5194/acp-15-3647-2015>
- Noll, S., Kausch, W., Kimeswenger, S., Unterguggenberger, S., & Jones, A. M. (2016). Comparison of VLT/X-shooter OH and O₂ rotational temperatures with consideration of TIMED/SABER emission and temperature profiles. *Atmospheric Chemistry and Physics*, *16*(8), 5021–5042. <https://doi.org/10.5194/acp-16-5021-2016>
- Noll, S., Kimeswenger, S., Proxauf, B., Unterguggenberger, S., Kausch, W., & Jones, A. M. (2017). 15 years of VLT/UVES OH intensities and temperatures in comparison with TIMED/SABER data. *Journal of Atmospheric and Solar-Terrestrial Physics*, *163*, 54–69. <https://doi.org/10.1016/j.jastp.2017.05.012>
- Noll, S., Plane, J. M. C., Feng, W., Proxauf, B., Kimeswenger, S., & Kausch, W. (2019). Observations and modeling of potassium emission in the terrestrial nightglow. *Journal of Geophysical Research: Atmospheres*, *124*(12), 6612–6629. <https://doi.org/10.1029/2018JD030044>
- Noll, S., Proxauf, B., Kausch, W., & Kimeswenger, S. (2018b). Mechanisms for varying non-LTE contributions to OH rotational temperatures from measurements and modelling. I. Climatology. *Journal of Atmospheric and Solar-Terrestrial Physics*, *175*, 87–99. <https://doi.org/10.1016/j.jastp.2018.05.004>
- Noll, S., Proxauf, B., Kausch, W., & Kimeswenger, S. (2018a). Mechanisms for varying non-LTE contributions to OH rotational temperatures from measurements and modelling. II. Kinetic model. *Journal of Atmospheric and Solar-Terrestrial Physics*, *175*, 100–119. <https://doi.org/10.1016/j.jastp.2018.05.005>
- Noll, S., Schmidt, C., Kausch, W., Bittner, M., & Kimeswenger, S. (2022a). Data for the paper “Effective emission heights of various OH lines from X-shooter and SABER observations of a passing quasi-2-day wave” [Dataset]. Zenodo. <https://doi.org/10.5281/zenodo.7371927>
- Noll, S., Schmidt, C., Kausch, W., Bittner, M., & Kimeswenger, S. (2022b). Effective emission heights of various OH lines from X-shooter and SABER observations of a passing quasi-2-day wave. *Journal of Geophysical Research: Atmospheres*, *127*(24), e2022JD036610. <https://doi.org/10.1029/2022JD036610>
- Noll, S., Schmidt, C., Kausch, W., Bittner, M., & Kimeswenger, S. (2023). Data for the paper “Climatologies of various OH lines from about 90,000 X-shooter spectra” [Dataset]. Zenodo. <https://doi.org/10.5281/zenodo.7826060>
- Noll, S., Winkler, H., Goussev, O., & Proxauf, B. (2020). OH level populations and accuracies of Einstein-A coefficients from hundreds of measured lines. *Atmospheric Chemistry and Physics*, *20*(9), 5269–5292. <https://doi.org/10.5194/acp-20-5269-2020>
- Oliva, E., Origlia, L., Scuderi, S., Benatti, S., Carleo, I., Lapenna, E., et al. (2015). Lines and continuum sky emission in the near infrared: Observational constraints from deep high spectral resolution spectra with GIANO-TNG. *Astronomy & Astrophysics*, *581*, A47. <https://doi.org/10.1051/0004-6361/201526291>
- Palo, S. E., Roble, R. G., & Hagan, M. E. (1999). Middle atmosphere effects of the quasi-two-day wave determined from a General Circulation Model. *Earth Planets and Space*, *51*(7–8), 629–647. <https://doi.org/10.1186/BF03353221>
- Pedatella, N. M., & Forbes, J. M. (2012). The quasi 2 day wave and spatial-temporal variability of the OH emission and ionosphere. *Journal of Geophysical Research*, *117*(A1), A01320. <https://doi.org/10.1029/2011JA017186>
- Pertsev, N., & Perminov, V. (2008). Response of the mesopause airglow to solar activity inferred from measurements at Zvenigorod, Russia. *Annals of Geophysics*, *26*(5), 1049–1056. <https://doi.org/10.5194/angeo-26-1049-2008>
- Preusse, P., Eckermann, S. D., Ern, M., Oberheide, J., Picard, R. H., Roble, R. G., et al. (2009). Global ray tracing simulations of the SABER gravity wave climatology. *Journal of Geophysical Research*, *114*(D8), D08126. <https://doi.org/10.1029/2008JD011214>
- Reid, I. M., Spargo, A. J., & Woithe, J. M. (2014). Seasonal variations of the nighttime O(1S) and OH(8-3) airglow intensity at Adelaide, Australia. *Journal of Geophysical Research: Atmospheres*, *119*(11), 6991–7013. <https://doi.org/10.1002/2013JD020906>
- Reisin, E. R., & Scheer, J. (2004). Gravity wave activity in the mesopause region from airglow measurements at El Leoncito. *Journal of Atmospheric and Solar-Terrestrial Physics*, *66*(6–9), 655–661. <https://doi.org/10.1016/j.jastp.2004.01.017>
- Rousselot, P., Lidman, C., Cuby, J.-G., Moreels, G., & Monnet, G. (2000). Night-sky spectral atlas of OH emission lines in the near-infrared. *Astronomy & Astrophysics*, *354*, 1134–1150.
- Russell, J. M., III, Mlynczak, M. G., Gordley, L. L., Tansock, J., & Esplin, R. (1999). Overview of the SABER experiment and preliminary calibration results. In A. M. Larar (Ed.), *Optical spectroscopic techniques and instrumentation for atmospheric and space research III* (Vol. 3756, pp. 277–288). <https://doi.org/10.1117/12.366382>
- Schmidt, C., Dunker, T., Lichtenstern, S., Scheer, J., Wüst, S., Hoppe, U.-P., & Bittner, M. (2018). Derivation of vertical wavelengths of gravity waves in the MLT-region from multispectral airglow observations. *Journal of Atmospheric and Solar-Terrestrial Physics*, *173*, 119–127. <https://doi.org/10.1016/j.jastp.2018.03.002>
- Schmidt, C., Höppner, K., & Bittner, M. (2013). A ground-based spectrometer equipped with an InGaAs array for routine observations of OH(3-1) rotational temperatures in the mesopause region. *Journal of Atmospheric and Solar-Terrestrial Physics*, *102*, 125–139. <https://doi.org/10.1016/j.jastp.2013.05.001>
- Sedlak, R., Zuhr, A., Schmidt, C., Wüst, S., Bittner, M., Didebulidze, G. G., & Price, C. (2020). Intra-annual variations of spectrally resolved gravity wave activity in the upper mesosphere/lower thermosphere (UMLT) region. *Atmospheric Measurement Techniques*, *13*(9), 5117–5128. <https://doi.org/10.5194/amt-13-5117-2020>
- Shepherd, M. G., Liu, G., & Shepherd, G. G. (2006). Mesospheric semiannual oscillation in temperature and nightglow emission. *Journal of Atmospheric and Solar-Terrestrial Physics*, *68*(3–5), 379–389. <https://doi.org/10.1016/j.jastp.2005.02.029>
- Smith, A. K. (2012). Global dynamics of the MLT. *Surveys in Geophysics*, *33*(6), 1177–1230. <https://doi.org/10.1007/s10712-012-9196-9>
- Smith, A. K., Marsh, D. R., Mlynczak, M. G., & Mast, J. C. (2010). Temporal variations of atomic oxygen in the upper mesosphere from SABER. *Journal of Geophysical Research*, *115*(D18), D18309. <https://doi.org/10.1029/2009JD013434>
- Swenson, G. R., & Gardner, C. S. (1998). Analytical models for the responses of the mesospheric OH* and Na layers to atmospheric gravity waves. *Journal of Geophysical Research*, *103*(D6), 6271–6294. <https://doi.org/10.1029/97JD02985>
- Takahashi, H., Clemesha, B. R., & Batista, P. P. (1995). Predominant semi-annual oscillation of the upper mesospheric airglow intensities and temperatures in the equatorial region. *Journal of Atmospheric and Terrestrial Physics*, *57*(4), 407–414. [https://doi.org/10.1016/0021-9169\(94\)E0006-9](https://doi.org/10.1016/0021-9169(94)E0006-9)
- Takahashi, H., Gobbi, D., Batista, P. P., Melo, S. M. L., Teixeira, N. R., & Burity, R. A. (1998). Dynamical influence on the equatorial airglow observed from the South American sector. *Advances in Space Research*, *21*(6), 817–825. [https://doi.org/10.1016/S0273-1177\(97\)00680-7](https://doi.org/10.1016/S0273-1177(97)00680-7)
- Tapping, K. F. (2013). The 10.7 cm solar radio flux (F10.7). *Space Weather*, *11*(7), 394–406. <https://doi.org/10.1002/swe.20064>
- Tunbridge, V. M., Sandford, D. J., & Mitchell, N. J. (2011). Zonal wave numbers of the summertime 2 day planetary wave observed in the mesosphere by EOS Aura Microwave Limb Sounder. *Journal of Geophysical Research*, *116*(D11), D11103. <https://doi.org/10.1029/2010JD014567>
- Vadas, S. L., Xu, S., Yue, J., Bossert, K., Becker, E., & Baumgarten, G. (2019). Characteristics of the quiet-time hot spot gravity waves observed by GOCE over the Southern Andes on 5 July 2010. *Journal of Geophysical Research: Space Physics*, *124*(8), 7034–7061. <https://doi.org/10.1029/2019JA026693>

- Vargas, F., Swenson, G., Liu, A., & Pautet, D. (2016). Evidence of the excitation of a ring-like gravity wave in the mesosphere over the Andes Lidar Observatory. *Journal of Geophysical Research: Atmospheres*, *121*(15), 8896–8912. <https://doi.org/10.1002/2016JD024799>
- Vernet, J., Dekker, H., D'Odorico, S., Kaper, L., Kjaergaard, P., Hammer, F., et al. (2011). X-shooter, the new wide band intermediate resolution spectrograph at the ESO Very Large Telescope. *Astronomy & Astrophysics*, *536*, A105. <https://doi.org/10.1051/0004-6361/201117752>
- von Savigny, C., McDade, I. C., Eichmann, K.-U., & Burrows, J. P. (2012). On the dependence of the OH* Meinel emission altitude on vibrational level: SCIAMACHY observations and model simulations. *Atmospheric Chemistry and Physics*, *12*(18), 8813–8828. <https://doi.org/10.5194/acp-12-8813-2012>
- Walterscheid, R. L., Hecht, J. H., Vincent, R. A., Reid, I. M., Woithe, J., & Hickey, M. P. (1999). Analysis and interpretation of airglow and radar observations of quasi-monochromatic gravity waves in the upper mesosphere and lower thermosphere over Adelaide, Australia (35°S, 138°E). *Journal of Atmospheric and Solar-Terrestrial Physics*, *61*(6), 461–478. [https://doi.org/10.1016/S1364-6826\(99\)00002-4](https://doi.org/10.1016/S1364-6826(99)00002-4)
- Zhang, S. P., Roble, R. G., & Shepherd, G. G. (2001). Tidal influence on the oxygen and hydroxyl nightglows: Wind Imaging Interferometer observations and thermosphere/ionosphere/mesosphere electrodynamics general circulation model. *Journal of Geophysical Research*, *106*(A10), 21381–21394. <https://doi.org/10.1029/2000JA000363>